Breakup of a leaky dielectric drop in a uniform electric field

Qingming Dong and Amalendu Sau*
Department of Aerospace and Software Engineering, Gyeongsang National University, Jinju 660701, South Korea

(Received 4 August 2018; revised manuscript received 15 March 2019; published 18 April 2019)

Electrohydrodynamic (EHD) breakup phenomena for a leaky dielectric drop suspended in another immiscible viscous dielectric and subjected to a uniform electric field are examined using the leaky dielectric theory and the explicit forcing lattice Boltzmann method, by taking into account full nonlinear inertia effects. The breakup modes are first computed for varied conductivity of the drop fluid, as the viscosity ratio λ ($=\mu_{in}/\mu_{out}$) is momentarily set to unity, that is, for the slightly conducting ($R = \sigma_{in}/\sigma_{out} < 10$), moderately conducting ($10 \leqslant R \leqslant 20$), and highly conducting ($R > 20$) cases. For slightly conducting drops ($R = 5$) only one breakup mode via two symmetrical necks persists for permittivity ratios $0.05 < Q = \varepsilon_{in}/\varepsilon_{out} < 3.0$ and electric capillary number $\mathrm{Ca}_E > \mathrm{Ca}_{E,\mathrm{critical}}$ (ratio of electric and surface tension forces), despite significant length-scale variation of mother and daughter drops. At higher Q (for increased drop permittivity) two necks move closer to the bulbous midpart of the extended droplet, which helps enlarge two daughter drops. However, in the case of moderately conducting drops ($10 \leqslant R \leqslant 20$) the number of necks increased to four for increased Ca_E. Accordingly two pairs of symmetrical daughter drops are created because of recurrent fluctuations of the electrical shear stress and centerline momentum flux. For highly conducting cases of $R > 20$, depending on Ca_E, three distinctly elongated droplet states are formed prior to breakup, which results in the onset of three different breakup modes, namely, via formations of lobed ends ($\mathrm{Ca}_E \leqslant 0.264$), pointed ends ($\mathrm{Ca}_E \leqslant 0.68$), and nonpointed ends ($\mathrm{Ca}_E > 0.83$). While being consistent with past measurements, here we precisely characterize the associated breakup mechanisms and physics in terms of the interactive electric pressure, electric shear stress, and hydrodynamic pressure plus velocity gradients. Since the EHD drop breakup is a dynamic process, on an elongated slender drop the activated locally distinct driving forces, i.e., *electric pressure at the end regions* and *tangential electric stress in the midsection*, effectively lead to neck formations by virtue of the created high centerline velocity gradient. Accordingly, resulting variations of local extension rate and net mass flux toward drop ends or into intermediate bulbous regions facilitate the multiple-mode drop breakup via the inertia effect, whereas the developed negative curvature around a neck encourages capillary breakup. We also explicitly reveal the effect of the viscosity contrast λ, which particularly influences the breakup characteristics over a broader range of conductivity ratios.

DOI: 10.1103/PhysRevE.99.043106

I. INTRODUCTION

The dynamical characteristic and breakup of a liquid drop in another immiscible liquid when exposed to an electric field play important roles and are widely encountered in many practical applications including ink-jet printing [1], electrospraying and atomization [2,3], enhancing heat or mass transfer between droplets and surrounding medium [4,5], flow manipulation in microdevices [6], light scattering, and birefringence and optical measurement of emulsions [7,8]. In earlier works, two extreme limits were widely considered in that a droplet is regarded as a perfect dielectric or a perfect conductor suspended in an insulating medium. Thereby only normal electric stress that acts on a drop surface is balanced by the surface tension, and at equilibrium the droplet elongates to a *prolate* shape in the direction of the applied electric field, while two fluids remain motionless. The phenomenon has been investigated [2,7,9,10] since the theoretical electrostatic framework was established, exhibiting that beyond a critical electric field strength the unstable drop breakup occurs. For the perfectly dielectric case (e.g., bubbles) the conical edges and shapes are formed at the droplet ends [11–13] prior to breakup, and then a series of small droplets is ejected from pointed tips [11]. For a perfectly conducting (water) drop, first Taylor [2] experimentally visualized the pointed tip formation and calculated the cone angle. Subsequently, Torza *et al.* [14] observed a new breakup mode of water drops in a uniform electric field in which the drop stretches to form two bulbous ends that remain connected by thin threads, and then gradually disintegrate into two bigger daughter droplets and a series of tiny ones. Recently, Ha and Yang [15] experimentally examined the breakup of aqueous conducting drops that are suspended in immiscible oil, and report a result consistent with that of Torza *et al.* [14], whereby the bulbous end-pinching mechanism leads to the droplet burst. However, the pointed end jet type structure of Taylor's [2] was not found by Ha and Yang [15]. Afterward using the Stokes flow approximation and the boundary integral method (BIM) Dubash and Mestel [16,17] studied the onset of breakup modes for a conducting drop in a viscous insulating fluid subjected to varied electric field strengths, and showed that as a droplet evolves up to breakup (above a critical field strength) three characteristic shapes are formed prior to disintegration:

*amalendu.sau@gmail.com

namely, a lobed end, a jetlike pointed end, and a nonpointed end, depending on viscosity ratio λ ($=\mu_{in}/\mu_{out}$) and electric capillary number Ca_E ($=E^2 a\varepsilon_{out}/\gamma$, where E, a, ε_{out}, γ denote magnitudes of uniform electric field, droplet radius, permittivity of outer medium, and surface tension). Later, following Dubash and Mestel's [16,17] work, Karyappa *et al.* [18] experimentally predicted the above three typical breakup modes for conducting drops. For $\lambda > 1$ only the pointed end mode is observed at all Ca_E above a critical value, whereas for lower λ ($<10^{-3}$) the drop breakup via lobe formation occurred. Within $10^{-2} < \lambda < 10^{-1}$ the breakup modes transit from the lobe formation to nonpointed ends to pointed ends, with increased Ca_E. However, an in-depth understanding or analysis of the precise roles of physically important interactive forces still eludes researchers, and notably the evolution of the breakup modes for a leaky drop is yet to be investigated or characterized using the fully nonlinear theory.

Besides an ideal situation (perfectly dielectric or conducting drops), realistically, most fluids have finite conductivity (well known as leaky dielectrics) as Taylor [19] noted. Due to the unequal variation of electric current between inside and outside, the significant net charge accumulates on a drop surface. Consequently, in addition to electric pressure, the tangential electric stress that acts on an interface drags the surrounding viscous fluid to motion and imposes important interfacial hydrodynamic stress and paired vortex dynamics directed forcing. Accordingly, depending on the interactive electric and hydrodynamic stresses, apart from the prolate deformation that was predicted by electrostatic theory [2], *oblate* or even *spherical* drop shapes are also formed [14,19]. Notably, Taylor's electrohydrodynamic (EHD) theory describes the physical phenomena in the limit of creeping flow and small perturbation from sphericity; later a complete framework (well known as the leaky dielectric model) for investigating the finite conducting drops was proposed by Melcher and Taylor [20]. However, when compared to the experiments of Torza *et al.* [14], Vizika and Saville [21], and Ha and Yang [15], Taylor's theory quantitatively underestimate the drop-deformation rate in a stronger electric field and is able to predict qualitatively the resulting deformation behavior. On the other hand, although Ajayi's [22] extended theory by taking into account higher-order corrections can better predict drop deformation over a broader range of electric field strength, the discrepancy between theory and experiment still remains.

In past years various linearized theoretical investigations have been performed to predict EHD behavior of a dielectric drop. Based on the Stokes flow assumption and BIM, Sherwood [12] studied the formation of various electric field strength–dependent elongated stable droplet shapes (at $\lambda = 1$) and their approach to the breakup modes for varying inner and outer fluid permittivity and conductivity. Notably, Sherwood [12] reveals the onset of two types of breakup modes for the dielectric drops: formation of pointed ends (that occurs prior to the tip streaming) for permittivity ratio ($Q = \varepsilon_{in}/\varepsilon_{out} \gg 1$) much greater than unity, and formation of the bulbous ends which remain connected by a thin thread for conductivity ratio $R = \sigma_{in}/\sigma_{out} \gg 1$. Following Sherwood's [12] work, Lac and Homsy [23] studied various possible limiting approaches for drop-breakup modes in the framework of the leaky dielectric model and examined the effect of viscosity contrast on a droplet's stability. Nevertheless, due to the restricting Stokes flow assumption [23] only stable deformation shapes or rates prior to breakup could be predicted instead of precise breakup process and crucial inner physics. Notably, for the considered Stokes flows *the time dependence acts only via the imposed kinematic boundary condition* on a drop. Meanwhile using the creeping flow assumption and the boundary element method (BEM) Baygents *et al.* [24] investigated the EHD interaction of a pair of leaky dielectric drops in an aligned electric field.

Distinctively, by relaxing the creeping flow condition and based on the *steady* Navier-Stokes equation, Feng and Scott [25] numerically studied stable (*nonbreaking*) deformation characteristics and electrically induced flow behavior for a leaky dielectric drop, and examined the influences of inertial force and drop viscosity. Recently, a number of numerical methods [13,26–29] based on the Navier-Stokes equations are proposed for computing deformation of a dielectric drop in a uniform electric field. However, such studies mostly address nonbreaking or limiting deformation scenarios below a threshold that provides an overview of possible droplet shapes in elongated states. Accordingly, despite academically enriching diverse approaches, the precise inner physics leading to the unstable growth, the actual breakup pattern, and the postbreaking evolution of a leaky drop by and large are still unaddressed, as previous works concentrate on the limiting approach to breakup. On the other hand, Ha and Yang [15] experimentally report various breakup modes for dielectric drops and growth of multiple pinching necks with increased drop viscosity, but clearly left enough room for categorical exploration of the driving inner physics that can unfold the crucial roles of the locally active tangential and normal electric stress and momentum flux or pressure gradient. As a whole, comprehensive knowledge on the diverse breakup mechanisms and governing inner physics for a leaky drop is therefore still lacking. Importantly, Collins *et al.* [30] recently examined the tip streaming mechanism for EHD jets, often referred to as electrospray, and proposed that the tangential electric stress can be vital for the tip streaming from drop ends. It is noteworthy that the phenomenon exists only in leaky dielectrics and did not occur when liquids are perfectly conducting or perfectly dielectric. In addition, Nganguia *et al.* [31] elaborate on the importance of the nonlinear inertial effects on EHD interaction of a viscous drop and show that interfacial distribution of the interactive electric stress plays a critical role in accurate prediction of a droplet pinch-off, whereas the linear Stokes flow approximation *significantly underestimates* the active electric pressure at poles.

The available literature [2,3,7,8,11–18] thereby shows the breakup of the perfectly conducting drops is relatively well studied, and viscosity ratio λ has a key role [16–18] to play in influencing different breakup patterns. Nevertheless, a systematic investigation plus thorough understanding of the breakup behavior or physics for the leaky dielectric drops are still lacking. Accordingly, the objectives of the present work are to (i) demonstrate the actual breakup mechanisms, (ii) explain the relevant physics in the framework of leaky dielectric fluids, and (iii) provide an inclusive overview of various breakup modes over a wide range of electric properties. Additionally, the drop breakup is strongly influenced by

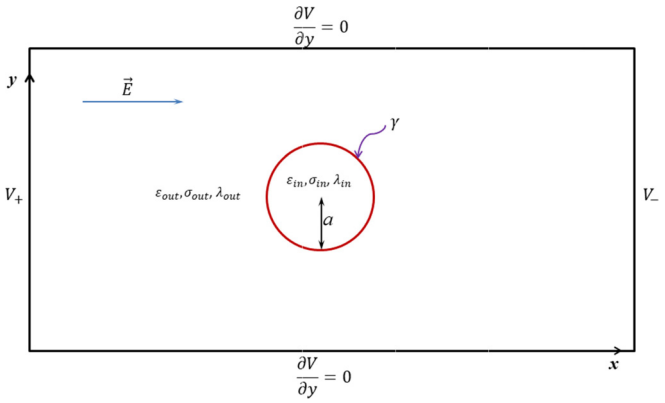

FIG. 1. Schematic of a leaky dielectric drop of radius a suspended in another immiscible leaky dielectric fluid and subjected to a uniform electric field $\vec{E}$.

coupled interaction of electric field and induced fluid motion, an unstable dynamic process. Inspired by the existing information [12,15,18] on breaking of conducting drops and lack of adequate results and clear understanding for leaky ones, in this work, with integrated full nonlinear inertia effects, we demonstrate different breaking patterns and governing physics for the suspended leaky dielectric drops, and examine the influence of varied viscosity contrast.

II. GOVERNING EQUATIONS AND NUMERICAL METHOD

We consider an uncharged liquid drop (Fig. 1) of radius a, placed in an immiscible fluid subjected to a uniform electric field $\vec{E}$. The liquids inside and outside are assumed incompressible (of equal density ρ), Newtonian, and leaky dielectrics [20,23–29], and have viscosities μ_{in}, μ_{out}, permittivities ε_{in}, ε_{out}, and conductivities σ_{in}, σ_{out}. The interface separating two immiscible fluids has constant surface tension γ. In the numerical framework adopted hereby we ignore the impacts of the buoyancy effect; however, the full nonlinear EHD interactions [26,31] are taken into account to reveal the actual drop-breakup modes and the physics.

A. Leaky dielectric model

The leaky dielectric theory [19,20] is used here to model the electrical response of a suspended drop in a surrounding fluid medium. While ignoring the magnetic induction effect, the EHD equations elaborated below become an accurate approximation. Since the propagation time for electromagnetic waves is much faster compared to the characteristic timescale of induced hydrodynamic motion, the small ionic charges are assumed present only at the interface, and the concept of diffuse (Debye) layers (volumetric charges) becomes irrelevant. Accordingly, the electrical phenomena are governed by

$$\nabla \times \vec{E} = 0. \tag{1}$$

Gauss's law in a dielectric fluid of permittivity ε, when written in terms of the electric displacement $\vec{D}$ $(=\varepsilon\vec{E})$, becomes the following [Eq. (2)]; wherein q_v denotes the volume density of free charge.

$$\nabla \cdot \vec{D} = \nabla \cdot (\varepsilon \vec{E}) = q_v. \tag{2}$$

In addition, the charge conservation equation is expressed as

$$\nabla \cdot \vec{J} + \frac{dq_v}{dt} = \nabla \cdot (\sigma \vec{E}) + \frac{\partial q_v}{\partial t} + \vec{u} \cdot \nabla q_v = 0, \tag{3}$$

where $\vec{J} = \sigma\vec{E}$ is the current density due to conduction, σ is the electrical conductivity, d/dt denotes the material derivative, and $\vec{u}$ is the local fluid velocity. From Eqs. (2) and (3), one can obtain

$$q_v = q_{v,0} e^{-\frac{\sigma}{\varepsilon}t}, \tag{4}$$

where the subscript 0 denotes initial time, and a field variable χ (σ or ε) corresponds to both χ_{in} and χ_{out}.

Equation (4) indicates that the charge density in the neighborhood of a fluid particle decays with relaxation time $t_e = \varepsilon/\sigma$. The hydrodynamic timescale for the motion is given by $t_v = \rho R^2/\mu$. Based on Melcher and Taylor's theory [20], for a conductive fluid with $t_e \ll t_v$, any existing free charge instantly accumulates at the interface and charge conservation occurs faster than fluid response. Consequently, for the leaky model, the free charge in bulk fluid is zero and the charge is constrained to the surface; i.e., $dq_v/dt = 0$, and Eq. (3) becomes

$$\nabla \cdot (\sigma \vec{E}) = 0. \tag{5}$$

Moreover, in terms of the electric potential (V), the electric field strength can be written as

$$\vec{E} = -\nabla V. \tag{6}$$

Combining Eqs. (5) and (6), the governing equation for the electric field (potential) becomes

$$\nabla \cdot (\sigma \nabla V) = 0. \tag{7}$$

On a fluid-fluid interface the electric potential (V) and the tangential component of the local electric field ($\vec{E}$) are assumed continuous, that is,

$$\vec{t} \cdot \vec{E}_{\text{in}} = \vec{t} \cdot \vec{E}_{\text{out}}, V_{\text{in}} = V_{\text{out}}, \tag{8}$$

where $\vec{t}$ is the unit tangent vector at the interface.

Note that, owing to mismatching electric properties of inner vs outer fluid, the jump of the ($\vec{E}_n$) normal component of the local electric field generates surface charge $q(\vec{x})$ that is calculated through Gauss's law,

$$q(\vec{x}) = [\![\varepsilon \vec{E}_n]\!] \quad \text{for } \vec{x} \in S, \tag{9}$$

where, $[\![\cdot]\!]$ denotes jump across an interface S. In relevant past works [23,26,28,31–33] two methods were employed to describe surface charge development. One method takes into account Ohmic currents from bulk and advection by fluid flow and is governed [30,32,33] by the following charge conservation equation,

$$\frac{\partial q}{\partial t} + [\![\sigma \vec{E}_n]\!] + \nabla_S \cdot (q\vec{v}) = 0 \quad \text{for } \vec{x} \in S, \tag{10}$$

where ∇_S is the gradient operator and $\vec{v}$ is the fluid velocity on the surface. The second method neglects the unsteady term and the surface charge convection [23–29,31]; Eq. (10)

thereby reduces to the simpler surface condition, that is, the continuity of the current,

$$[\![\sigma \vec{E}_n]\!] = 0. \tag{11}$$

The EHD phenomenon arises due to the persisting electric stress at the interface. However, the electric forces are essentially exerted on interfacial free charges and charge dipoles rather than on the dielectric fluid. Therefore, the electric body force ($\vec{F}_E$) can be described [20,33] in terms of divergence of the Maxwell stress, $\vec{\sigma}_M = \varepsilon \vec{E}\vec{E} - \frac{\varepsilon}{2}[1 - \frac{\rho}{\varepsilon}(\frac{\partial \varepsilon}{\partial \rho})]E^2\, \boldsymbol{I}$, where $\boldsymbol{I}$ is the identity tensor, and $\vec{F}_E$ coupled with hydrodynamic and surface tension forces drives the EHD flow in a medium of continuously varying permittivity and bulk charges. The electric force ($\vec{F}_E$) per unit volume, as calculated by taking the divergence of the Maxwell stress tensor, becomes

$$\vec{F}_E = \nabla \cdot \vec{\sigma}_M = q_v \vec{E} - \frac{1}{2}\vec{E} \cdot \vec{E}\nabla\varepsilon + \nabla\left(\frac{1}{2}\vec{E} \cdot \vec{E}\frac{\partial \varepsilon}{\partial \rho}\rho\right). \tag{12}$$

Assuming incompressibility and inserting electric body force together with surface tension force into the Navier-Stokes equations, one obtains the governing equations [26,28] for the EHD flow phenomena, known as the leaky dielectric model. The relevant boundary conditions at the interfaces are the continuity of velocity, $\vec{u}_{\text{in}} = \vec{u}_{\text{out}}$; and balancing the jump in total stress and interfacial tension, i.e., $[\![\vec{n} \cdot \vec{T}^H]\!] = \gamma\kappa\vec{n} - [\![\vec{n} \cdot \vec{T}^E]\!]$, where $\kappa = [(\boldsymbol{I} - \vec{n}\,\vec{n}) \cdot \nabla] \cdot \vec{n}$ is the interfacial mean curvature.

Over the past years the response of an *isolated leaky dielectric drop* suspended in an immiscible leaky dielectric medium and subjected to a uniform electrostatic field has been widely examined [13,20,23–33]. Due to interactive interfacial stresses, the drop experiences "prolate" or "oblate" deformation [34]. The resulting drop deformation D in terms of fluid properties is expressed as [13,14,20,23–33]

$$D = \frac{L - B}{L + B} = \frac{9 f_d}{16(2 + R)^2}\text{Ca}_E, \tag{13}$$

$$f_d = R^2 + 1 - 2Q + \frac{3}{5}(R - Q)\frac{(2 + 3\lambda)}{(1 + \lambda)}, \tag{14}$$

where L is the end-to-end length of a deformed drop measured along the applied electric field, B is the maximum drop width perpendicular to the electric field, and f_d is the discriminating function. For $f_d > 0$, a drop deforms into the prolate form, and when $f_d < 0$ the drop assumes the oblate shape.

B. Numerical method and its implementation

1. Explicit forcing interparticle potential lattice Boltzmann method

Recently Porter *et al.* [35] proposed an improved explicit forcing lattice Boltzmann (LB) model, where the forcing term is directly incorporated into the discrete Boltzmann equation. In the present work, we implemented below the LB model of Porter *et al.* [35] to simulate the EHD interactions, as it is verified [34,36] to be substantially upgraded on various fronts and is quite effective. The LB model is expressed as

$$\begin{aligned} f_l^k(\vec{x} + \vec{e}_l\Delta t,\ t + \Delta t) - f_l^k(\vec{x},\ t) &= -\frac{f_l^k(\vec{x},\ t) - f_l^{k(eq)}\left(n_k, \vec{u}_k^{eq}\right)}{\tau^k} \\ &\quad + \Delta t\left(1 - \frac{1}{2\tau^k}\right)\frac{\left(\vec{e}_l - \vec{u}_k^{eq}\right) \cdot \vec{F}_k}{\rho_k c_s^2}\, f_l^{k(eq)}\left(n_k, \vec{u}_k^{eq}\right), \end{aligned} \tag{15}$$

where $f_l^k(\vec{x},\ t)$ is the probability distribution function of the kth component in the direction of the lth molecular velocity ($\vec{e}_l$) at $\vec{x}$ at time t, and τ_k is the nondimensional relaxation time. As evidenced below, the adopted D2Q9 [34,35,37] model efficiently and accurately predicts the multiphase EHD interactions. In the above, $f_l^{k(eq)}(n_k, \vec{u}_k^{eq})$ representing local Maxwellian equilibrium distribution is given by [29,35–38]

$$\begin{aligned} f_0^{k(eq)} &= \alpha_k n_k - \frac{2}{3}n_k\vec{u}_k^{eq} \cdot \vec{u}_k^{eq}, \\ f_l^{k(eq)} &= \frac{(1 - \alpha_k)n_k}{5} + \frac{1}{3}n_k\left(\vec{e}_l \cdot \vec{u}_k^{eq}\right) + \frac{1}{2}n_k\left(\vec{e}_l \cdot \vec{u}_k^{eq}\right)^2 \\ &\quad - \frac{1}{6}n_k\vec{u}_k^{eq} \cdot \vec{u}_k^{eq}, \quad \text{for} \quad l = 1 - 4, \\ f_l^{k(eq)} &= \frac{(1 - \alpha_k)n_k}{20} + \frac{1}{12}n_k\left(\vec{e}_l \cdot \vec{u}_k^{eq}\right) + \frac{1}{8}n_k\left(\vec{e}_l \cdot \vec{u}_k^{eq}\right)^2 \\ &\quad - \frac{1}{24}n_k\vec{u}_k^{eq} \cdot \vec{u}_k^{eq}, \quad \text{for} \quad l = 5 - 8, \end{aligned} \tag{16}$$

and the discrete molecular velocity $\vec{e}_l$ are expressed as

$$\vec{e}_l = \begin{pmatrix} \vec{0}, & l = 0, \\ \left[\cos\frac{(l-1)\pi}{2},\ \sin\frac{(l-1)\pi}{2}\right], & l = 1 - 4, \\ \sqrt{2}\left\{\cos\left[\frac{(l-5)\pi}{2} + \frac{\pi}{4}\right],\ \sin\left[\frac{(l-5)\pi}{2} + \frac{\pi}{4}\right]\right\}, & l = 5 - 8 \end{pmatrix}. \tag{17}$$

The parameter α_k in Eq. (16) is related to the speed of sound in the D2Q9 model [37], and is given by $(c_s^k)^2 = 0.6(1 - \alpha_k)$. n_k is the total number of density of the kth component, defined by $n_k = \sum_l f_l^k$. Moreover, the mass density of the kth component, $\rho_k = m_k n_k = m_k \sum_l f_l^k$, where m_k is the kth molecular mass. The kth component of the fluid velocity $\vec{u}_k^{eq}$ at equilibrium state is therefore determined by

$$\vec{u}_k^{eq} = \left(\sum_{k=0}^{s}\frac{\rho_k\vec{u}_k}{\tau_k}\right)\Big/\left(\sum_{k=0}^{s}\frac{\rho_k}{\tau_k}\right), \tag{18}$$

$$\rho_k\vec{u}_k = \sum_l f_l^k\vec{e}_l + 0.5\Delta t\ \vec{F}_k, \tag{19}$$

where $S+1$ represents the total number of components in the multiphase system, and $\vec{F}_k$ is the total force acting on the kth component, including fluid-fluid interaction ($\vec{F}_k^{\text{int}}$) and electric ($\vec{F}_k^{\text{ele}}$) forces, as appropriate for this work.

For the interparticle potential model, the interactive force between particles of the kth component at $\vec{x}$ and the $\bar{k}$th component at $\vec{x}'$ is assumed [34,35,37] proportional to the product of their *effective number density* $\varphi_k(n_k)$, defined as a function of local number density. Following past investigations [29,37,39], $\varphi_k(n_k)$ is chosen here as n_k. Therefore, the total interaction force acting on the kth component at $\vec{x}$ is given by

$$\vec{F}_k^{\text{int}}(\vec{x}) = -n_k(\vec{x}) \sum_{x'} \sum_{\bar{k}} G_{k\bar{k}}(\vec{x},\vec{x}')\, n_{\bar{k}}(\vec{x}')\, (\vec{x}-\vec{x}'). \quad (20)$$

In Eq. (20) above, $G_{k\bar{k}}(\vec{x},\vec{x}')$ is the Green's function that satisfies $G_{k\bar{k}}(\vec{x},\vec{x}') = G_{\bar{k}k}(\vec{x},\vec{x}')$, the magnitude of which controls the strength ($g_{k\bar{k}}$) of the interaction potential. For the adopted D2Q9 lattice arrangement, we follow a method similar to that proposed by Martys and Chen [40] to obtain the required interaction potential by projecting the four-dimensional face-centered hypercubic (4D FCHC) lattices to the present D2Q9 format. Accordingly, the potential that couples nearest and next nearest neighbors becomes

$$G_{k\bar{k}}(\vec{x},\vec{x}') = \begin{Bmatrix} g_{k\bar{k}}, & |\vec{x}-\vec{x}'| = 1 \\ \frac{g_{k\bar{k}}}{4}, & |\vec{x}-\vec{x}'| = \sqrt{2} \\ 0, & \text{otherwise} \end{Bmatrix} \quad (21)$$

The whole fluid velocity ($\vec{u}$) is thereby expressed in the following form,

$$\vec{u} = \frac{\sum_k \rho_k \vec{u}_k}{\sum_k \rho_k}, \quad (22)$$

and the kinematic fluid viscosity is expressed as

$$\upsilon = \frac{1}{3}\sum_k \frac{\rho_k \tau_k}{\rho} - \frac{1}{6}. \quad (23)$$

Therefore, for the kth component, the viscosity is reduced to

$$\upsilon = \tfrac{1}{3}\tau_k - \tfrac{1}{6}. \quad (24)$$

2. *LBM approach for computing electric field and treatment of interface*

Notably, the electric potential equation, Eq. (7), is an elliptic equation, while LBM is a method that essentially solves the parabolic equation. Thus, the solution of Eq. (7) is conveniently obtained (He and Li [41]; Guo *et al.* [42]) as the steady solution of the following equation [Eq. (25)] in the LBM timescale.

$$\frac{\partial V}{\partial t} + \nabla\cdot(\sigma \nabla V) = 0. \quad (25)$$

Hereby, the new particle distribution function h_l is introduced [41,42] and expressed as

$$h_l(\vec{x} + \vec{e_l}\,\Delta t,\ t+\Delta t) - h_l(\vec{x},\ t) = -\frac{h_l(\vec{x},\ t) - h_l^{eq}(\vec{x},\ t)}{\tau^h}. \quad (26)$$

The corresponding equilibrium distributions h_l^{eq} and the relaxation time τ_h are expressed as

$$h_0^{eq} = \tfrac{4}{9}V, \quad h_l^{eq} = \tfrac{1}{9}V, \quad l = 1-4, \quad (27a)$$

$$h_l^{eq} = \tfrac{1}{36}V, \quad l = 5-8, \quad \tau_h = 3\sigma + 0.5, \quad (27b)$$

where σ represents a combination of electric conductivities, as described below. Based on Eqs. (26) and (27), Eq. (25) can be recovered using the Chapman-Enskog expansion [43], while the electric potential V is defined as

$$V = \sum_l h_l. \quad (28)$$

Note that the influence of the electric field in EHD motion activates through the Maxwell's stress that develops due to different fluid conductivity and permittivity and/or electric field strength. In numerical algorithms solving two-phase hydrodynamics (see Kang *et al.* [39]), the sharp interface is often treated as a diffused one spanning over a thin region (of three grid sizes [28,39]), where physical properties continuously and smoothly transit from a value of one phase to that of another phase [34]. The electric force that exists only on the interface is induced by the nonuniform electric properties (σ and ε). In this context, to derive an equivalent electric volume force representation [i.e., Eq. (29) given below] for Eq. (12) the work of Tomar *et al.* [28] that follows the continuum surface tension model of Brackbill *et al.* [44] is employed, which effectively calculates the surface force in the transition region of the inhomogeneous fluid system.

$$\vec{F}_E = 0.5\left\{\nabla\left(\frac{\epsilon}{\sigma^2}\right)[\sigma(\vec{E}\cdot\vec{n})]^2 - (\vec{E}\cdot\vec{t})^2\nabla\epsilon\right\} + \left[(\sigma\vec{E})\cdot\nabla\left(\frac{\epsilon}{\sigma}\right)\right](\vec{E}\cdot\vec{t})\vec{t}, \quad (29)$$

where the normal vector $\vec{n}$ is defined as $\vec{n} = \nabla(\epsilon/\sigma)/|\nabla(\epsilon/\sigma)|$; ϵ, σ are the dielectric permittivity and conductivity in the transition region. To calculate the electric force $\vec{F}_E$ for the transition region, the dielectric properties need to be interpolated. For this, a weighted harmonic mean [Eq. (30)] interpolation scheme [28] is suitably adopted here, in which the electric field strength ($\vec{E}$) remains independent of the interface thickness.

$$\frac{\rho}{\varepsilon} = \frac{\rho_{\text{in}}}{\varepsilon_{\text{in}}} + \frac{\rho_{\text{out}}}{\varepsilon_{\text{out}}}, \quad \frac{\rho}{\sigma} = \frac{\rho_{\text{in}}}{\sigma_{\text{in}}} + \frac{\rho_{\text{out}}}{\sigma_{\text{out}}}, \quad (30)$$

and $\rho(=\rho_{\text{in}} + \rho_{\text{out}})$ denotes the total density for the mixture.

Furthermore, to deal with two different fluids the electric force $\vec{F}_E$ [Eq. (29)] is needed to split into two parts and be properly applied for each set of fluid properties. We divide this force according to the density-ratio as

$$\vec{F}_k^{\text{ele}} = \frac{\rho_k}{\rho}\vec{F}_E, \quad k = 1,\ 2. \quad (31)$$

III. RESULTS AND DISCUSSION

Extensive simulations are now carried out in a two-dimensional (2D) physical ($32a \times 28a$) domain covered by 300×256 D2Q9 lattices, using the implemented periodic condition (Fig. 1) for fluid motion in both x and y directions. The EHD system that remains exposed to a uniform electric

field is created by maintaining the (constant) higher and lower electric potential at left (V_+) and right (V_-) boundaries of the domain (Fig. 1), and the Neumann type spanwise condition ($\partial V/\partial y = 0$) for electric potential is employed along the y boundaries. The molecular mass (m_k) is set to be 1.0. To examine the influence of the electric field on the drop, the densities of the drop fluid and surrounding fluid are considered to be identical. Moreover, for the adopted explicit forcing LBM model the interaction potential strengths are appropriately [35] selected as $g_{12} = g_{21} = 0.275$, $g_{11} = g_{22} = 0.0$.

A. Computation of surface tension

To begin the investigation, we first calculate the surface tension γ [37,39] of a drop suspended in another fluid, which also helps to validate the adopted LB approach. For this, in the absence of electric field, a circular drop (of radius a) of one fluid is placed symmetrically in a domain filled with a second fluid. At equilibrium, the pressure jump ($p_{\text{in}} - p_{\text{out}}$) across the drop interface (in the absence of body force) is balanced by the surface tension pressure, and the evolution of the drop is governed [45] by Laplace's law,

$$p_{\text{in}} - p_{\text{out}} = \gamma/a, \tag{32}$$

whereas the pressure p for the whole fluid domain is expressed as [37]

$$p = \frac{1}{3}\sum_k n_k + \frac{3}{2}\sum_{k\bar{k}} g_{k\bar{k}} n_k n_{\bar{k}}. \tag{33}$$

Using 300×256 square lattices, the initial density for component 1 was set as 2.0 in the drop and 0.01 for the outer fluid, whereas the density for component 2 was initially set to be 0.01 for the drop and 2.0 elsewhere. Accordingly, simulations for the multicomponent fluid flow with different component densities are conducted with varied drop radius a and the resulting pressure difference $p_{\text{in}} - p_{\text{out}}$ is computed at the steady state. Since the LBM is a dynamical procedure, the static state for the drop is achieved through the time-evolution of about 15 000 time steps. Figure 2 presents the computed $p_{\text{in}} - p_{\text{out}}$ for varied a, together with the fitted solid line that obeys the Laplace equation [Eq. (32)]. Accordingly, the computed slope, i.e., the surface tension, becomes $\gamma = 0.27$. The linear fit, in Fig. 2, between computed $p_{\text{in}} - p_{\text{out}}$ and $1/a$ is clearly consistent with the Laplace equation.

B. Validation of the explicit forcing LBM model

For comparison, at this stage we first compute stable equilibrium deformation (D) of a leaky dielectric drop in another immiscible fluid subjected to a uniform electric field that is below the threshold of breakup ($\text{Ca}_E < \text{Ca}_{E,\text{critical}}$). The liquid properties inside and outside a drop are taken identical to cases $Q = 0.1, 1.37, 5.0$, at $R = 10$ and $\lambda = 1$, those used by Lac and Homsy [23]; in addition, the results for $Q = 0.1$ correspond to those of Nganguia *et al.* [31]. Following Feng and Scott [25], the Reynolds numbers Re ($=au/\nu_{\text{out}}$) for EHD flows are calculated based on the maximum interface velocity, $u = \frac{9a\,\varepsilon_{\text{in}}E_\infty^2}{10\,\mu_{\text{in}}}\,[|\frac{R}{Q} - 1\,|/(2+R)^2\,(1+\frac{1}{\lambda})]$. Figure 3 shows the computed Ca_E-dependent drop deformation D [Eqs. (13) and (14)] using the present nonlinear flow model, and creeping flow solution of Lac and Homsy [23] and the Navier-Stokes solution of Nganguia *et al.* [31]. Important to note in Fig. 3 is that the linear dependence of D and E^2 (as $\text{Ca}_E \sim E^2$) in the form of constant dD/dE^2 slope [Eq. (9)] that satisfies Taylor's linear theory is valid for $D < 0.1$, and for $D > 0.1$ the dependence reveals nonlinear behavior. In addition, dD/dE^2 rapidly increases, especially for lower Q(=0.1, 1.37) cases for which a slight increase of Ca_E causes a sudden drop elongation, as drops transit from ellipsoidal to extended slender two-lobed shapes. To be precise, a quick shape transition at $Q = 1.37$ as shown in the inset (in Fig. 3) is detected for a small increase of the Ca_E from 0.383 57 to 0.385 57. In

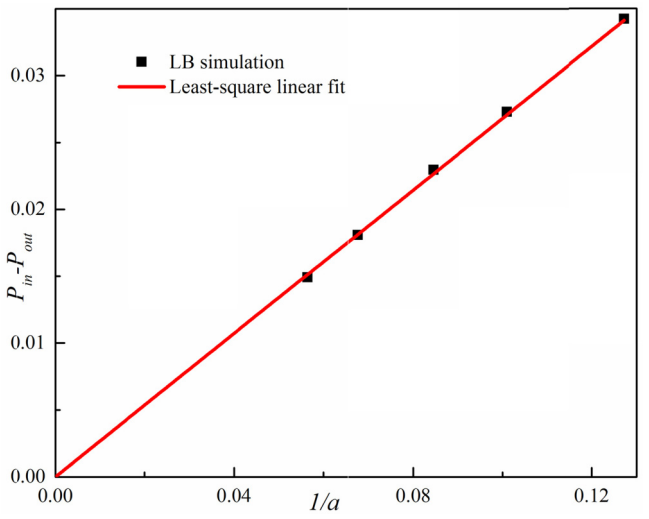

FIG. 2. Computed surface tension for a single drop by Laplace's law. The slope (surface tension) is 0.27.

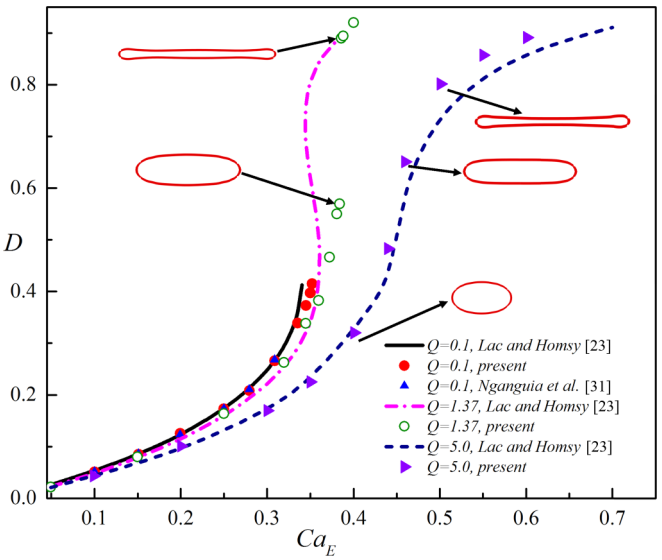

FIG. 3. Comparison of the present results, creeping flow solution of Lac and Homsy [23], and Navier-Stokes solution of Nganguia *et al.* [31] for the Ca_E-dependent stable drop deformation (D), as permittivity ratio Q is varied at fixed $R = 10$, $\lambda = 1$. Computed different cases are $Q = 0.1$ ($0.135 \leqslant \text{Re} \leqslant 0.46$), $Q = 1.37$ ($0.058 \leqslant \text{Re} \leqslant 0.468$), and $Q = 5.0$ ($0.0684 \leqslant \text{Re} \leqslant 0.411$).

contrast, for $Q = 5.0$, the increasing trend of dD/dE^2 appears rather slow and the drop gently evolves from an ellipsoidal to an elongated shape (when necks did not form) in the range $0.4 \leqslant \mathrm{Ca}_E \leqslant 0.5$. As Fig. 3 reveals, in the small deformation regime (for varied Q and $\mathrm{Ca}_E \leqslant 0.35$) the simulated D using the present nonlinear model is in good agreement with the Stokes flow (BIM) solution of Lac and Homsy [23] and the nonbreaking scenario ($Q = 0.1$) described by Nganguia *et al.* [31]. Nevertheless, the slight deviation with Lac and Homsy [23] occurs as a droplet undergoes larger deformation, possibly influenced due to the fact [25,31] that the BIM [23] ignores important inertial effects (for which $\mathrm{Re} = 0$), whereasthe lattice Boltzmann equation solved here is equivalent to nonlinear Navier-Stokes equations. The recent study by Nganguia *et al.* [31] clearly shows the discrepancy of D originates from gradually enhanced inertial force ($\mathrm{Re} > 0$) with increased Ca_E; although the effect depends on direction of the interactive normal electric stress [31]. More precisely, the locally developed positive electric pressure (pointed outward) leads to larger drop deformation and a negative electric pressure reverses the trend [31]. At $Q = 0.1$ (<1) the negative electric pressure (pointed inward) persists everywhere [Fig. 5(c2)] except at poles, whereas all along positive electric pressure [23] is induced at $Q = 5$. Therefore, it is rational that in larger deformation regimes the simulated D (Fig. 3) appears relatively larger than the Stokes flow solution [23] at $Q = 5$, and smaller at $Q = 0.1$, due to added inertial effect. However, the observed close variations of D (Fig. 3; $\mathrm{Re} > 0$) show that the adopted LBM model can correctly predict the EHD deformation behavior of a suspended drop. In addition, extensive validation of the model is presented in a recent work [34], revealing virtual coincidence of LBM solutions and those obtained by the level set [13] and volume of fluid [28] methods.

C. Drop-breakup modes for varied conductivity at fixed $\lambda = 1$

In this subsection we analyze breakup characteristics of the leaky drops with varied conductivity ratio (R) at $\lambda = 1$. Based on the elaborated diverse breakup modes, leaky drops are classified into three categories, namely, highly ($R > 20$) conducting, intermediately ($10 \leqslant R \leqslant 20$) conducting, and slightly ($R < 10$) conducting subclasses, and these terminologies are followed throughout. For clarity, a phase diagram in (R, Ca_E)-space is presented in Fig. 4, wherein the dashed line divides the entire parameter space into *stable deformation* and *unstable breakup* regimes. In the unstable regime different breakup modes are noted for varied parameter (R, Ca_E) combination. Following the transition patterns, the unstable regime is split into several specific subregimes that facilitate breakup via a single pair of necks (SPN), multiple pair of necks (MPN), lobe formation (LF), pointed end (PE), and non-pointed end (NPE), as illustrated in Fig. 4 and described below.

1. Breakup modes for a slightly conducting drop ($R < 10$)

Figure 5(a) presents the transient EHD deformation plus breakup behaviors of a *slightly conducting* drop with field properties $R = 5.0$, $Q = 0.05$, $\mathrm{Ca}_E = 1.3$. It shows, following EHD interaction, the suspended drop first transits to an ellipsoidal shape at $t = T$ ($T = 100$ lattice unit time) and then

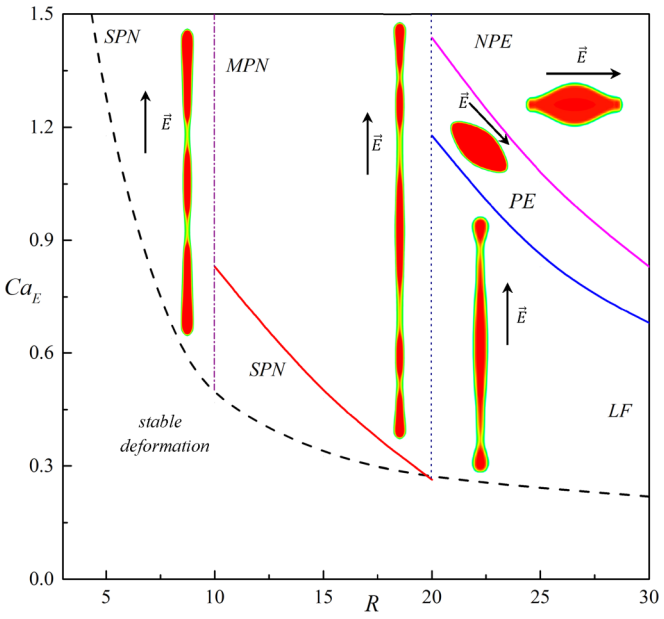

FIG. 4. Phase diagram for the EHD drop deformation and breakup in (R, Ca_E) space; $\lambda = 1$, $Q = 1.37$. The dashed line is the boundary between *stable* (lower region) and *unstable* deformation regimes. SPN and MPN denote single and multiple pairs of pinching neck. LF, PE, and NPE correspond to varying breakup modes via lobe formation, pointed end, and nonpointed end, respectively.

keeps stretching in the form of a slender cylinder. During the process clear formation of three bulbous regions take place at $t = 4.5T$; they are seen remaining temporarily connected by two thinner necks. Subsequently the two slender, cylinder shaped daughter droplets pinch off ($t \geqslant 5.5T$) from the mother droplet, and move toward oppositely charged edges ($t \geqslant 7T$) and relax to ellipsoidal shapes, whereas the relaxed similar sized mother droplet (e.g., at $t = 9.5T$) becomes eventually motionless by virtue of symmetrically imposed interfacial stresses [Figs. 5(c1) and 5(c2)].

To get a better insight into this drop-breakup phenomenon, Fig. 5(b1) shows important near-field flow characteristics at $t = 4.5T$, as neck formation appears clear. In Fig. 5(b1), note the significant variation of inertia that acts in different parts of the transitioning drop ($\mathrm{Re} = 2.58$) and the advection of two dominating outward moving, *outflow* natured [34] vortex pairs at left and right in the bulk fluid, which effectively drives the two end regions to stretch oppositely and separate away from the mother drop, via the imposed interfacial thrust. Accordingly three distinct drop regions [Fig. 5(b1)] are clearly formed prior to breakup ($t = 4.5T$): the midsection $1.32 < x < 1.68$, and two symmetric end regions at left ($x < 1.2$) and right ($x > 1.8$); they remain connected by two thin liquid threads in neck regions $1.2 < x < 1.32$ and $1.68 < x < 1.8$. Figures 5(b1) and 5(b3) reveal the persistence of the crucial horizontal (u) velocity gradient along the centerline of the stretched drop. Notably, distinctly from cases associated with a perfectly conducting drop [15,18] or an insulating dielectric drop suspended in an insulating medium, for the leaky drop in addition to the electric pressure (normal electric stress) the induced surface charge generates significant tangential electric stress that drives [19,20,33] the near-field

hydrodynamics in Fig. 5(b1). For clarity, Figs. 5(c1) and 5(c2) present the detailed variation of the interactive tangential and normal electric stresses along the droplet surface [Fig. 5(b1)] at $t = 4.5T$. Figure 5(c1) shows the antisymmetrical rapid fluctuation and enhancement of the tangential stress near the drop ends ($x < 0.95$ or $x > 2.05$), whereas precisely at the end points it reduces to zero owing to the symmetric end shape, clarifying that at the poles the droplet stretching is driven by the positive (pointing from droplet to outer fluid) electric pressure [Fig. 5(c2)] that attained the local maximum. Physically, the surface charge accumulates near two tips ($x < 0.95$, $x > 2.05$) of a *slender* leaky dielectric drop, where rapid growth and variation of tangential and normal electric stresses occur [30]. Note in Fig. 5(c2) that at places away from the drop ends the negative electric pressure is generated for $Q = 0.05$ (<1), and the magnitude attains local

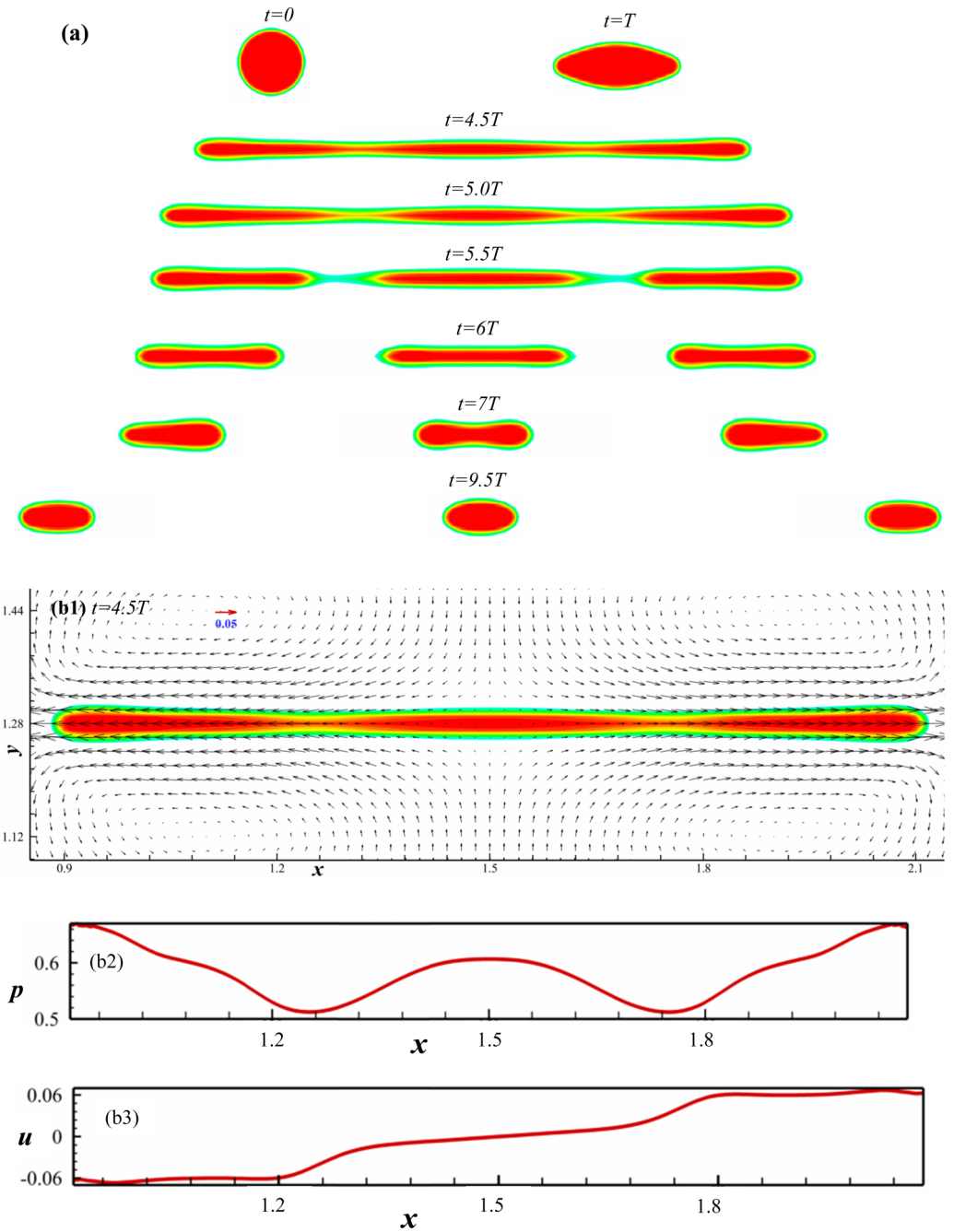

FIG. 5. (a) The time-dependent evolution and breakup process of the slightly conducting drop at $R = 5.0$, $Q = 0.05$, $\lambda = 1.0$, $\mathrm{Ca}_E = 1.3$, and $\mathrm{Re} = 2.58$. (b1) Near-field instantaneous flow behavior around an elongated droplet during neck formation; $t = 4.5T$; (b2), (b3) extracted pressure and velocity distribution along the drop centerline at $t = 4.5T$; (b4), (b5) profiles of cross-sectional u-velocity magnitude at $x = 1.45$ (representative of drop-midsection region) and $x = 0.98$ (represents drop-end region) at $t = 4.5T$. (c1), (c2) The nondimensional tangential electric stress and electric pressure distribution on drop surface at $t = 4.5T$. The tangential electric stress directed toward the left is taken as positive (*Continued.*).

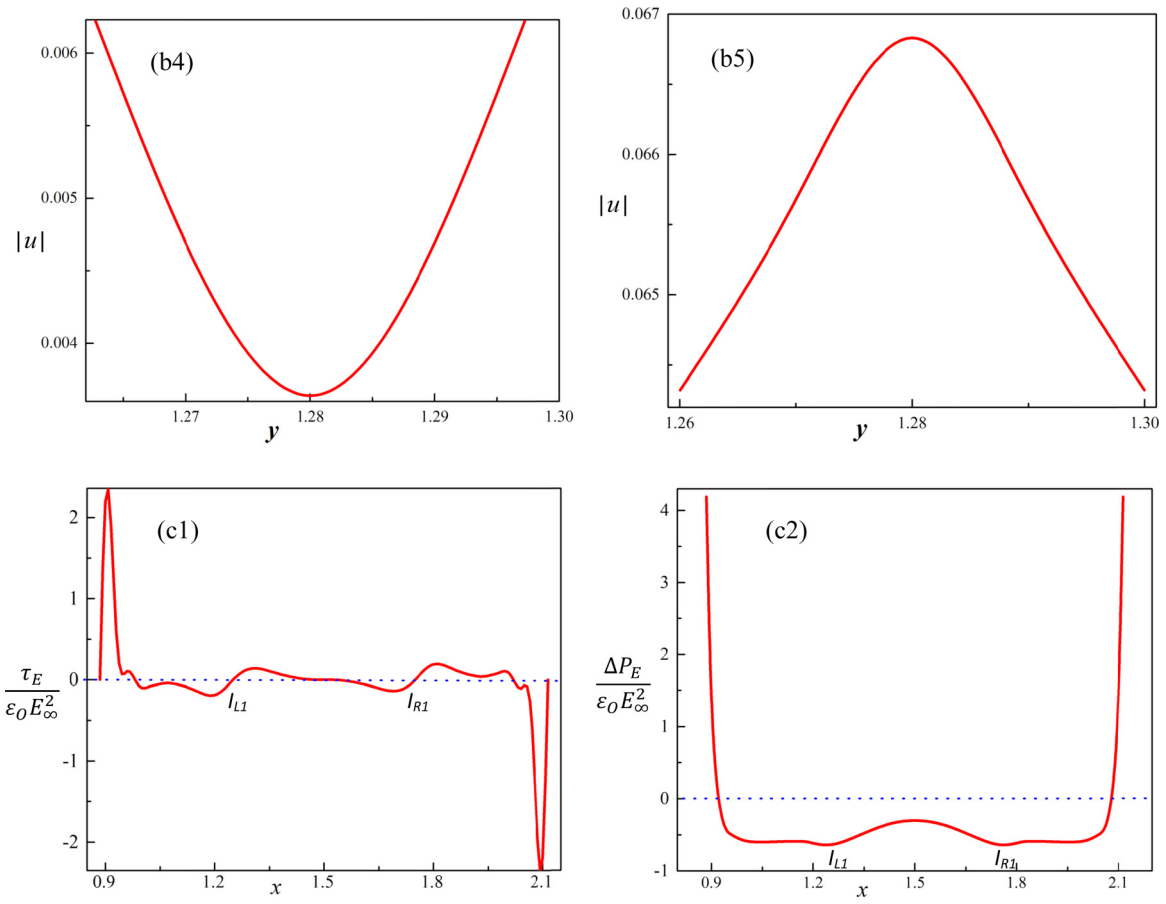

FIG. 5. (*Continued.*)

negative maximum precisely in two necks, at $x = 1.26(I_{L1})$ and $x = 1.74(I_{R1})$. Moreover, as evident from Fig. 5(c1), in two necks the tangential electric stress crosses the zero mark at the *inflection* (eventual breakup) *points* $I_{L1}(x = 1.26)$ and $I_{R1}(x = 1.74)$, while in the vicinity its oscillatory perturbation of opposite nature with high gradient is noteworthy. Importantly, for such an elongated droplet state the dominating sign (positive or negative) of electric pressure away from the end points depends on the permittivity ratio Q, which is noted to be positive [Fig. 6(c2)] for $Q > 1$, and negative for $Q < 1$ [Fig. 5(c2)]. One may think that the negative electric pressure plays a crucial role in droplet breakup, because it reduces the effect of the surface tension. Nevertheless, the direction of electric pressure (positive or negative) alone cannot determine the occurrence of droplet collapse, as the breakup of a leaky drop in elongation is a dynamic process that depends on the created local extension rate [23,30,46] owing to strong interaction between the electric field and the vortex induced flow field [Fig. 5(b1)]. Note in this context in Fig. 5(c1) the antisymmetric variation of the tangential electric stress with respect to the droplet center ($x = 1.5$), and its near-tip sudden reduction of magnitude to zero. Hereby, the tangential electric stress directed toward the left is defined as positive. However, the tangential electric stress alone cannot decisively dictate droplet deformation; it acts to impact surrounding fluid motion through the viscosity effect [30].

To better predict the physical mechanism leading to the droplet breakup, Figs. 5(b2) and 5(b3) shows the crucial changes of internal velocity (u) and pressure (p) along the drop centerline, at $t = 4.5T$, as the neck formation is taking place, providing clear insight for the nonuniform drop extension rates. First, note in the midsection $1.32 < x < 1.68$ the persisting significantly lower u, velocity [Fig. 5(b1)], having a small axial gradient [Fig. 5(b3)]. Second, within two end sections $x < 1.2$, $x > 1.8$ rather uniform but clearly higher (u) velocity is maintained (negative on the left and positive on the right side). Third, the phenomenally active higher velocity gradient persists [Fig. 5(b3)] in transitional and developing neck zones $1.2 < x < 1.32$ and $1.68 < x < 1.8$. The observed high velocity difference [Fig. 5(b3)] between the midsection and two end parts creates [30] the inertia-driven *distinct local extension rates* for a drop in the elongated state, leading to formation of neck regions. Moreover, the resulting net mass flux [Fig. 5(b1)] toward the drop ends is contributed by the persisting high velocity gradient in the necks; accordingly the necks become more and more thin and subsequent pinch-off [Fig. 5(a)] occurs at a certain point (for $t > 5T$). In the process, the created negative curvature around the necks leads to the development of the local low pressure regions, as clearly visible in Fig. 5(b2), which generates a bigger inner-outer pressure difference to facilitate capillary breakup, as explained by Collins *et al.* [30].

To clearly demonstrate the importance of imposed electric stress in inducing the essential variations of the internal flow mechanism that lead to breakup, Figs. 5(b4) and 5(b5) show the cross-sectional $|u|$ profiles at $x = 1.45$ (representative of

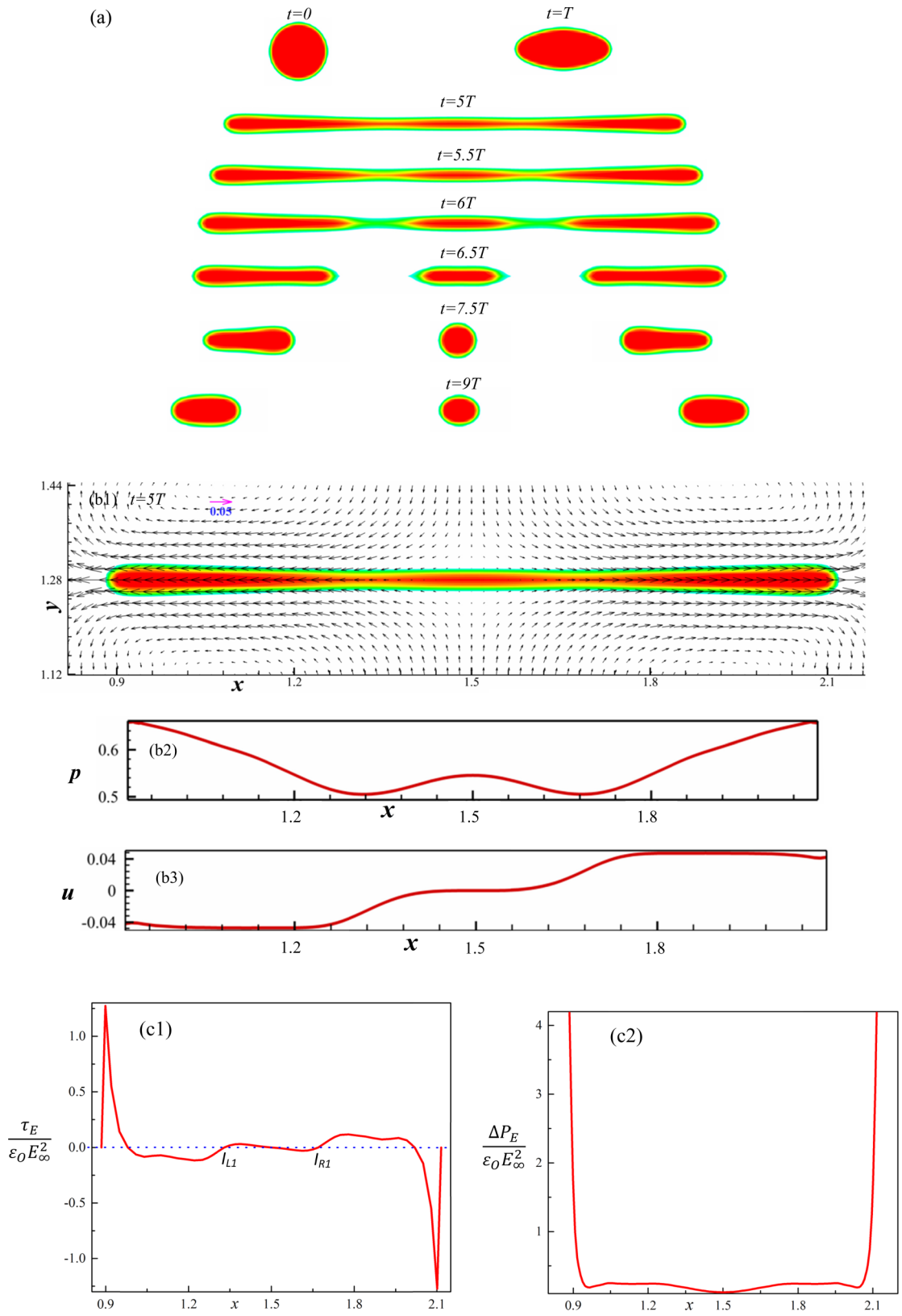

FIG. 6. Influence of Q (>1) on the breakup of a slightly conducting drop. (a) The time-dependent evolution of the drop shape in the breakup process at $R = 5$, $Q = 1.37$, $\lambda = 1$, $\mathrm{Ca}_E = 1.3$, and $\mathrm{Re} = 1.9$. (b1) Near-field instantaneous flow behavior around an elongated droplet during neck formation, $t = 5T$; (b2), (b3) extracted instantaneous pressure and velocity distribution along the drop centerline at $t = 5T$. (c1), (c2) The nondimensional tangential electric stress and electric pressure distribution on drop surface at $t = 5T$.

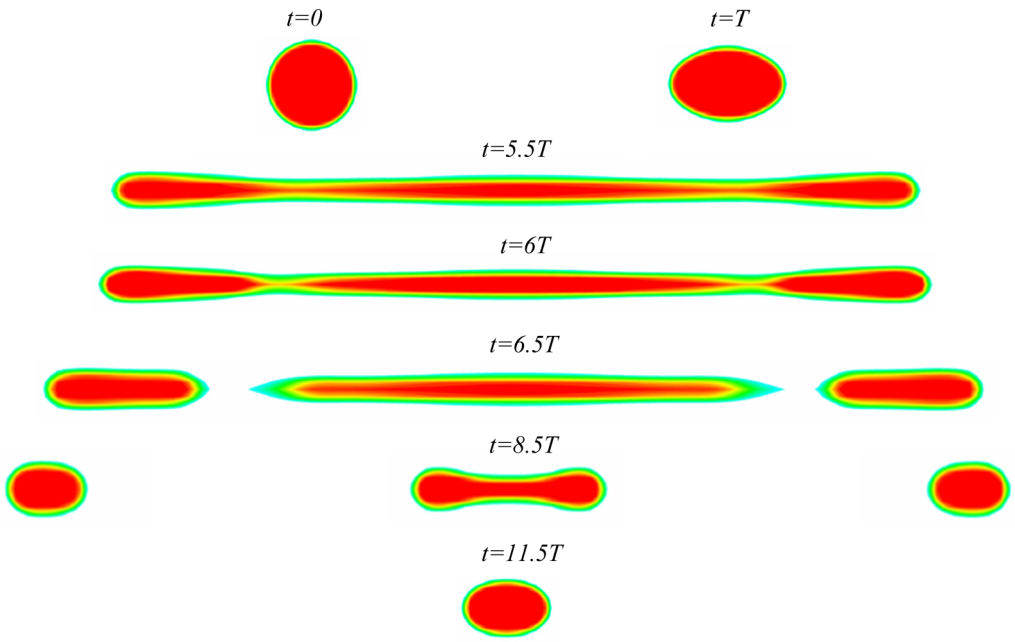

FIG. 7. Temporal evolution and breakup of an intermediately conducting drop at $R = 10$, $Q = 1.37$, $\lambda = 1$, $\mathrm{Ca}_E = 0.55$, and $\mathrm{Re} = 0.65$.

flow behavior in droplet midsection) and $x = 0.98$ (represents an end region). As seen in Fig. 5(b4), the velocity curve at $x = 1.45$ is strongly indicative of typical *shear stress-driven flow* (parabolic velocity profile) whereby the *minimum velocity* occurs at the *droplet centerline* ($y = 1.28$). Since the pressure gradient balances the viscous stress in shear stress-driven flows, in Fig. 5(b2) slowly decreasing p away from the midsection and along the drop centerline is induced. Accordingly the surface motion caused by interactive tangential electric stress [Fig. 5(c1)] drives the internal fluid to flow [30]. Distinctly, at $x = 0.98$, the maximum velocity [Fig. 5(b5)] in the cross section occurs at the droplet centerline ($y = 1.28$), showing that *close to tip regions* the significantly higher *normal electric stress* [electric pressure, Fig. 5(c2)] that is imposed by accrued charges effectively *dictates the internal fluid flow*, which overcomes a visibly higher local pressure gradient [Fig. 5(b2)]. Such issues have been noted in a pioneering work by Collins *et al.* [30].

Now, with fixed $R = 5$ and $\mathrm{Ca}_E = 1.3$, we increase the permittivity ratio Q to 1.37 (>1) and examine its influence on the drop breakup. At $Q = 1.37$, Fig. 6(a) shows the gradual drop evolution and later breakup into markedly different proportions with respect to those [Fig. 5(a)] at $Q = 0.05$. To be precise, for $Q = 1.37$ the neck regions $1.24 < x < 1.38$ and $1.64 < x < 1.78$ [see Fig. 6(b1)] move significantly close to the droplet center ($x \approx 1.5$) producing two larger daughter drops and one smaller mother drop for $t \geqslant 6.5T$, as noted in Fig. 6(a). However, the breakup of a leaky drop depends on the varying local extension rate determined by interaction between the electric field and the induced bulk fluid motion. To extract the physics leading to the breakup phenomenon at $Q = 1.37$, we analyze an instantaneous droplet state at $t = 5T$ [Fig. 6(b1)] following the neck formation. Figure 6(c2) shows that, in this case, the positive electric pressure persists on the whole drop surface, which could possibly inhibit the occurrence of breakup (and neck formation). However, the developed higher electric pressure at two tips still acts as the decisive driving force that supports the drop elongation. Accordingly, the resulting sudden increase or decrease of axial flow as seen in Figs. 6(b1) and 6(b3) reveals the crucial transitioning character of the internal flow; from the tangential electric stress driving in the midsection ($1.38 < x < 1.64$) to electric pressure driving at the two tips (drop-end regions; $x < 1.24$, $x > 1.78$). This occurs despite the fact that the magnitude of tangential electric stress [especially in the midpart, Fig. 6(c1)] is decreased significantly with increased permittivity ratio ($Q = 1.37$); the corresponding [Fig. 6(b3)] fluid velocity is also decreased. The presented distribution of tangential electric stress in Fig. 6(c1) shows the inflection points $I_{L1}(x = 1.31)$, $I_{R1}(x = 1.71)$, i.e., the eventual breakup points (where τ_E crosses zero) at this higher $Q(=1.37)$ have moved closer toward the drop center, resulting in formation of a smaller sized mother drop [Fig. 6(b1)].

2. *Breakup modes for intermediately conducting drop* ($10 \leqslant R \leqslant 20$)

For the increased conductivity ratio R, more electric charges accumulate on the drop surface. Accordingly, for a given electric field strength, the resulting higher electric stress reduces the critical electric capillary number ($\mathrm{Ca}_{E,\mathrm{critical}}$) that is required to facilitate the onset of drop breakup. To extract the related physics, we first compute two intermediately conducting drop-breaking cases at $R = 10$, using varied Ca_E. Figure 7 shows that the breaking behavior of an intermediately conducting drop ($R = 10$) at a lower $\mathrm{Ca}_E = 0.55$ is apparently consistent with those for the slightly conducting drops ($R = 5$, Figs. 5 and 6). However, the size of two daughter drops (Fig. 7, at $t \geqslant 6T$) clearly decreased (compared to slightly conducting cases, Figs. 5 and 6), as a larger fraction of mass stays in the midsection of an intermediately conducting drop with $10 \leqslant R \leqslant 20$. Moreover, quite distinctively from

slightly conducting drops ($R = 5$, Figs. 5 and 6) that exhibit breakup strictly via two necks (for $\mathrm{Ca}_E \geqslant \mathrm{Ca}_{E,\mathrm{critical}}$), Fig. 8 reveals that at an increased $\mathrm{Ca}_E = 0.83$ the intermediately conducting ($R = 10$) drop evolves through multiple pinching necks and eventually breaks into multiple pairs of daughter drops. Notably, Fig. 8(a) shows symmetric formation of four transitioning bulbous regions for $4T \leqslant t \leqslant 4.5T$ in two sides, in addition to one formed in the central part, by virtue of persisting locally nonuniform internal mass transport [Fig. 8(b1)] at $\mathrm{Ca}_E = 0.83$. At $t = 4T$ the bulbous masses remain connected [Fig. 8(a)] by thin necks, and at $t \geqslant 4.5T$ the resulting four daughter drops are seen to pinch off. Importantly, our simulated breaking pattern in Fig. 8 appears quite similar to the experimental results reported by Ha and Yang [15] in their Fig. 7 for $\lambda = 0.874$ (~ 1), despite the adopted nonlinear model being of 2D nature. As evidenced hereby, a consistent but enhanced variation of the inertia [e.g., larger velocity gradient, Fig. 8(b3)] driven local forcing for different bulbous sections of the transitioning drop [Fig. 8(b1)] in this case ($R = 10$, $\mathrm{Re} = 0.98$, $\mathrm{Ca}_E = 0.83$) leads to the observed multiple neck formations and resulting faster breakup ($t \geqslant 4.5T$).

It is enlightening to examine the corresponding governing physics, as the multiple neck formation takes [Fig. 8(a)] place. First, Figs. 8(b2) and 8(b3) reveal detailed pressure and velocity distributions along the droplet centerline at $t = 4T$. Notably, Fig. 8(b3) shows clear persistence of locally higher (u) velocity gradient within $0.9 < x < 0.98$ and $1.14 < x <$

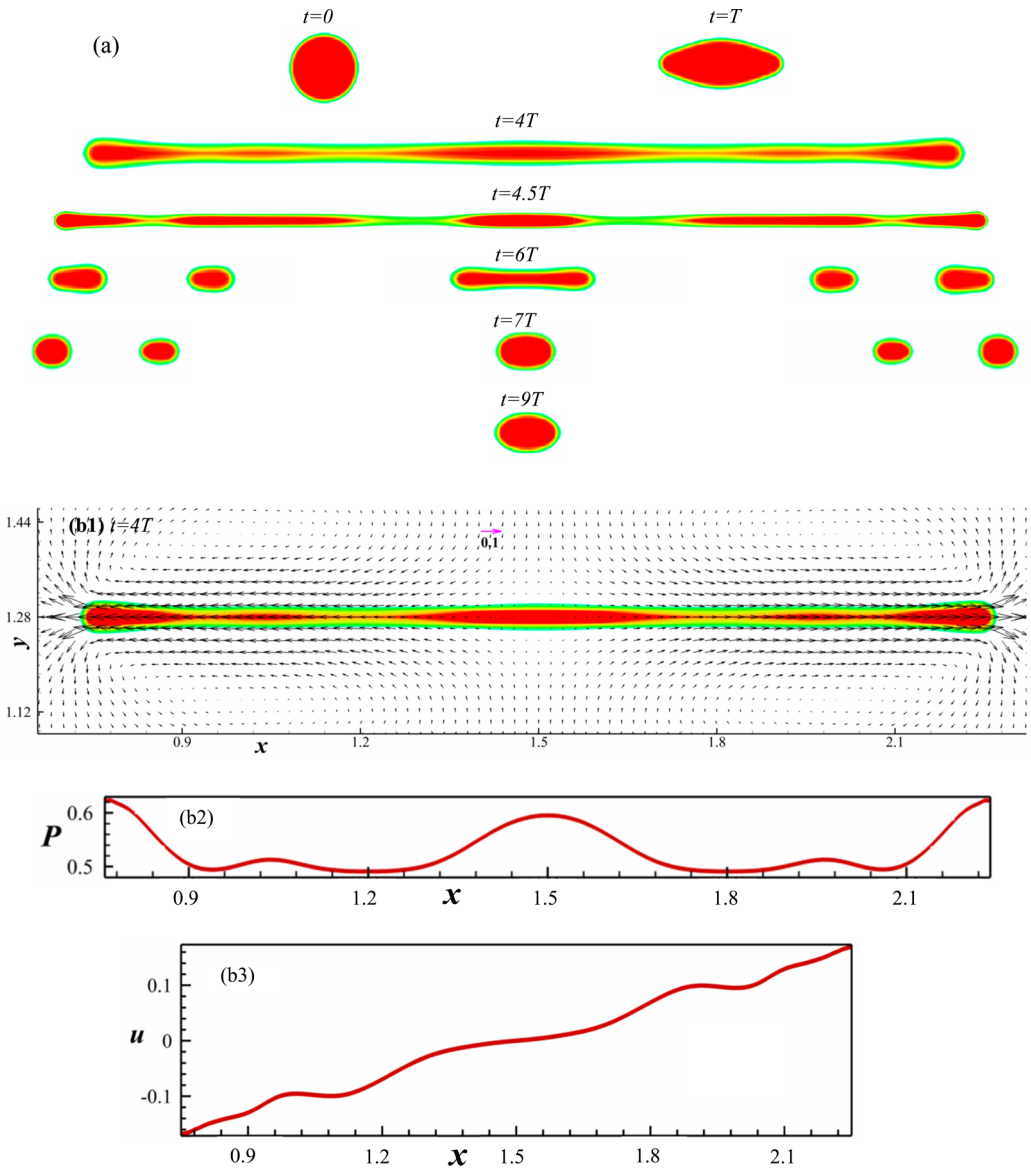

FIG. 8. Impact of increased Ca_E and resulting multicomponent breakup of an intermediately conducting drop. (a) Time-dependent drop shape evolution in the process of breakup at $R = 10$, $Q = 1.37$, $\lambda = 1$, $\mathrm{Ca}_E = 0.83$, and $\mathrm{Re} = 0.98$. (b1) The near-field flow behavior around an elongated drop during neck formation at $t = 4T$; (b2), (b3) extracted pressure and velocity distribution along the drop centerline at $t = 4T$. (b4)–(b6) Profiles of cross-sectional u-velocity magnitude at $x = 1.46$, $x = 1.04$, and $x = 0.78$; $t = 4T$. (c1), (c2) Distributions of nondimensional tangential electric stress and electric pressure on drop surface at $t = 4T$ (*Continued.*).

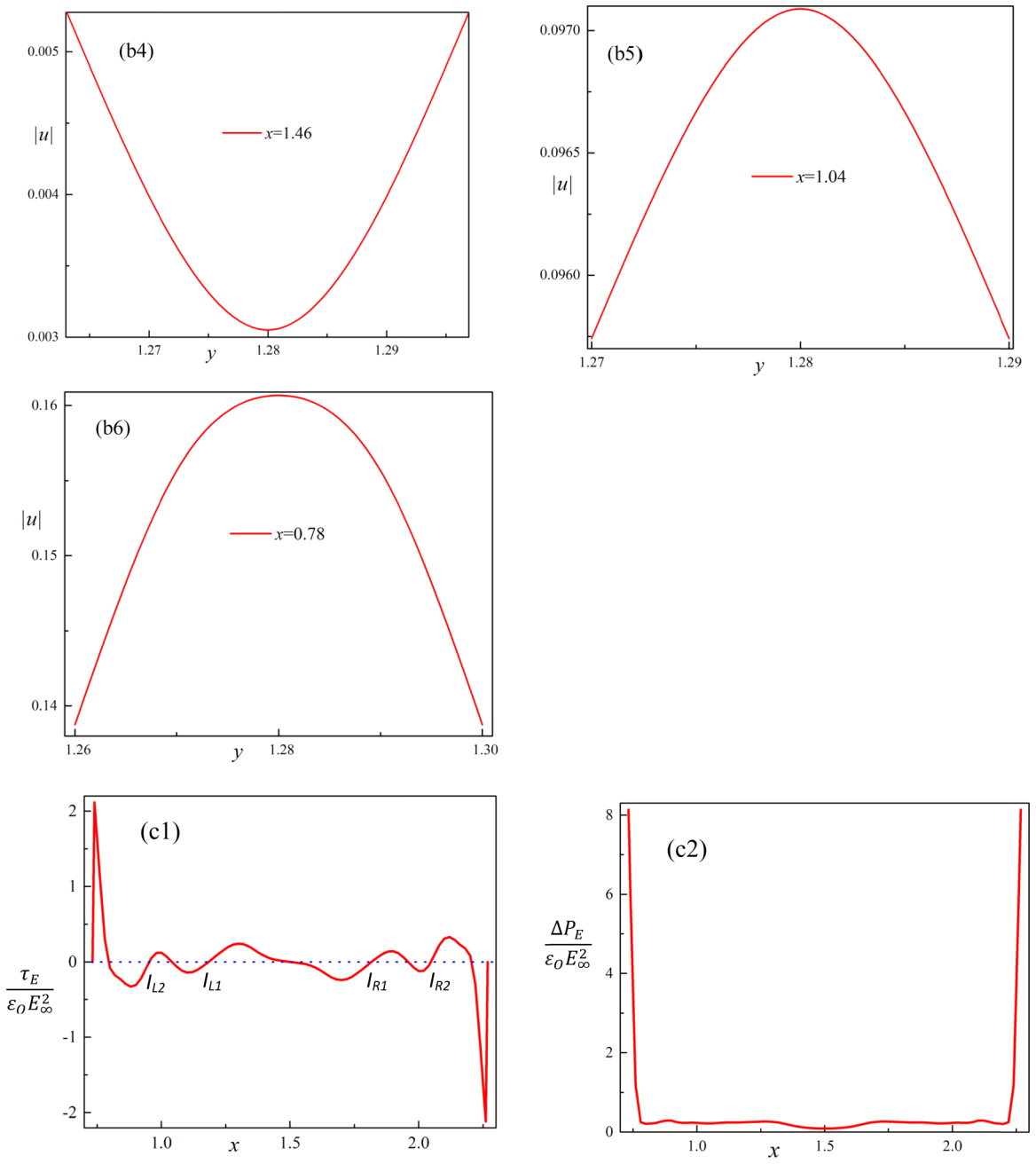

FIG. 8. (*Continued.*)

1.32, in two unequally extended necks in the left half ($x < 1.5$), and the existence of symmetrically developed similar velocity gradients in $1.68 < x < 1.86$ and $2.02 < x < 2.1$ in the right half ($x > 1.5$). Figures 8(c1) and 8(c2) show the distributions of interactive electric stress on the drop surface (at $t = 4T$). Note in this case [Fig. 8(c2), $R = 10$] the generated significantly higher electric pressure at two tips, with respect to slightly conducting drops [Figs. 5 and 6, $R = 5$], which effectively pulls two bulbous ends ($x < 0.9, x > 2.1$) to move left or right with visibly higher velocity [Fig. 8(b3)], and facilitates the formation of necks. Such distinctive forcing features persist despite the intermediately conducting (Fig. 8) drop is placed in a relatively weaker electric field ($\mathrm{Ca}_E = 0.83$) than slightly conducting drops ($\mathrm{Ca}_E = 1.3$, $R = 5$, in Figs. 5 and 6). Figures 8(b1) and 8(b3) show that two intermediate nearly uniform flow regions $0.98 < x < 1.14$ and $1.88 < x < 2.02$ of visibly low velocity gradient are formed between two end regions and the midsection, wherein the intermediate bulbous shapes develop. On either side the dominating steep velocity (u) gradient, by virtue of the high local extension rate within the necks, drastically reduces the net mass flux, which helps the creation of two inner daughter drops. Note in this context the appearance of two *additional* inflection points I_{L2} and I_{R2} in Fig. 8(c1), where the tangential electric stress crosses the zero mark, whereas for slightly conducting cases [Figs. 5(c1) and 6(c1)] they do not exist. To uncover the driving flow mechanisms, Figs. 8(b4)–8(b6) show the important cross-sectional u profiles. The u profiles at $x = 0.78$

[Fig. 8(b6)] and $x = 1.46$ [Fig. 8(b4)] unambiguously reveal that the dominating driving forces are the electric pressure in the end regions (where $|u|_{\max}$ occurs on the droplet axis), and tangential electric stress in the *midsection* (as $|u|_{\max}$ occurs on drop interfaces). Between the left end region and the midsection ($x = 1.5$) the noted formation of a u profile at $x = 1.04$ [Fig. 8(d5)] similar to that at $x = 0.78$ [Fig. 8(d6)] shows that the *inertia dictates the local flow dynamics* in the intermediate bulbous regions.

3. *Breakup modes for highly conducting drops ($R > 20$)*

For highly conducting drops of fixed $R = 30$ we first examine their evolution for varied $Q = 0.1,\ 1.37,\ 10.0$. Notably, at $R = 30$, the breakup behaviors presented in Figures 9 and 10 resemble that of widely reported [15–18] perfectly conducting drops, in that permittivity ratio Q seems to have little influence. Our computed critical $Ca_{E,c}$'s that initiates the onset of drop breakup in the above three cases are 0.219, 0.219, 0.227, respectively, which remain consistent to around 0.22 predicted by Lac and Homsy [23] for a highly conducting dielectric drop, and 0.23 experimentally found by Ha and Yang [15] for the NN1-16 (conducting) system. In addition, Ha and Yang [15] and Feng and Scott [25] report that an EHD drop can be treated as a perfectly conducting one for $R > 10^5$. Accordingly the investigated cases (at $R = 30$) in this section are still dielectrics that satisfy the leaky model [20]. Figure 9(a) illustrates the simulated detailed drop-breakup phenomenon at $R = 30$, $Q = 1.37$, $\lambda = 1$, $\mathrm{Ca}_E = 0.264$. Note that, for this highly conducting ($R = 30$) drop at low Ca_E, first, the final stretched length prior to breakup [Fig. 9(b1), at $t = 3.5T$] is significantly shorter compared to that at lower R [Figs. 5–8]. Second, Fig. 9(a) shows the consistent growth of the lobed ends prior to pinch-off that is experimentally observed by Karyappa *et al.* [18]. Third, in previous works [16–18] on *perfectly conducting drops*, the authors found such a breakup mode [Fig. 9(a)] via lobe formation at small viscosity ratio ($\lambda < 0.1$) and lower Ca_E ($\leqslant 0.3$). However, phenomenologically distinctive from the perfectly conducting cases, for the leaky drop [30] the accumulated charges induce crucial tangential electric stress on the surface. As Fig. 9(c1) shows, at both ends the generated higher tangential electric stress induces the growth of curved bulbous end shapes [30] for the leaky drop, instead of pointed ends noted by Sherwood [12] *for a conducting drop*. Additionally, at $R = 30$, an augmented charge accumulation on lobe ends results in the creation of significantly stronger local electric pressure, as noted in Fig. 9(c2), which is about four and two times higher, respectively, than slightly ($R = 5$) and moderately ($R = 10$) conducting drops placed in stronger electric fields [$\mathrm{Ca}_E = 1.3$ in Fig. 5(c2); $\mathrm{Ca}_E = 0.83$ in Fig. 8(c2)], whereas the highly conducting ($R = 30$) drop in Fig. 9 is placed in a weaker ($\mathrm{Ca}_E = 0.264$) electric field. Note also that, at $R = 30$, a stronger axial flow (u) is clearly created in the droplet, especially in end regions, as Fig. 9(b3) shows. Moreover the bulbous end shapes increase the local curvature around necks, resulting in formations of local low pressure regions [Fig. 9(b2)] in necks ($x \sim 1.12,\ x \sim 1.88$) that facilitate capillary breakup [Fig. 9(a)]. However, upon the pinch-off that produced the first pair of daughter drops (at $t = 4.5T$), similar bulbous growth and breakup processes are repeated, and the second and the third pairs of daughter drops are generated [see Fig. 9(a) for $t \geqslant 5.5T$], until the interactive tangential and normal electric stresses appear insufficient to further disintegrate the droplet. Eventually, the mother or central drop relaxes and approaches an asymptotic equilibrium shape, at $t = 9T$, whereas the daughter drops move toward distant edges. As Figs. 9(b1) and 9(b3) reveal, at $R = 30$, a stronger internal flow with high gradient is created via the imposed significantly higher electric stress [Figs. 9(c1) and 9(c2)], that causes the necks to move outward and closer to droplet ends and leads to small size daughter drop formation [Fig. 9(a)]. Noteworthy in Fig. 9(b1) are the dominating *outflow* paired outer vortex dynamics [34,47] near two bulbous ends, which effectively facilitate the axial drop stretching via their consistent opposite or outward directed induced motion. For additional clarity, the invariances of the simulated [Fig. 9(a)] daughter drop ejection and neck formation processes with implemented higher lattice resolution are revealed in Appendix.

With increased $\mathrm{Ca}_E > 0.66$, the lobes are noted to disappear for a highly conducting ($R = 30$) leaky drop, and such results seemed quite consistent with the theoretical predictions of Sherwood [12]. Hereby, two types of drop shapes developed prior to breakup: the pointed ends for $0.66 < \mathrm{Ca}_E < 0.83$ and the nonpointed end for $\mathrm{Ca}_E \geqslant 0.83$. Figures 10(a1) and 10(b1) elaborate the typical instantaneous droplet deformation processes at $\mathrm{Ca}_E = 0.68$ and 0.83 prior to breakup that maintained convex or oval shapes until the local highest curvature regions are developed at the drop ends. It is noteworthy that quite similar drop transition patterns from pointed to nonpointed ends are reported for the perfectly conducting drops [16–18] with increased Ca_E. For Stokes flow (using BIM) Sherwood [12] shows that at a large conductivity ratio $R > 28$ (and $Q = 1.0$) two ends of a leaky drop become pointed owing to enhancement of the normal electric stress at the tips. Additionally an air bubble (that corresponds to a perfectly dielectric case, in which only electric pressure exists on the interface) is reported [11] to develop the pointed ends prior to breakup, when placed in an electric field. The mechanism that leads to the formation of pointed ends is in fact dictated by the locally developed sufficiently stronger electric pressure near the tips. Notably, for the present *leaky dielectric drops* the imposed higher electric field ($\mathrm{Ca}_E > 0.66$) clearly augments [Fig. 10(a2)] the near-tip electric pressure. Considering that the drop breakup itself is a dynamic process, for balancing the developed gradually higher electric pressure with increased electric field strength (Ca_E) and to stabilize the droplet a sharper curvature is clearly formed [Fig. 10(a1)] in the high electric pressure regions [30]. Once the rate of increase of electric pressure exceeds the precision curvature change, the breakup occurs. For clarity, Fig. 10(a2) shows important local variation of the electric stress along the right upper-half drop interface at the onset of breakup, showing that the largest electric pressure is formed precisely at the tip, and thereby a pointed end develops [Fig. 10(a1)]. However, for increased $\mathrm{Ca}_E = 0.83$, Fig. 10(b2) shows that the maximum electric pressure is no longer located at the tip. Accordingly, on the left and right, the symmetrically developed highest electric pressure [e.g., at $x = 1.67$, Fig. 10(b2)] at the two largest curvature areas [that moved slightly inward, Fig. 10(b1)] helps

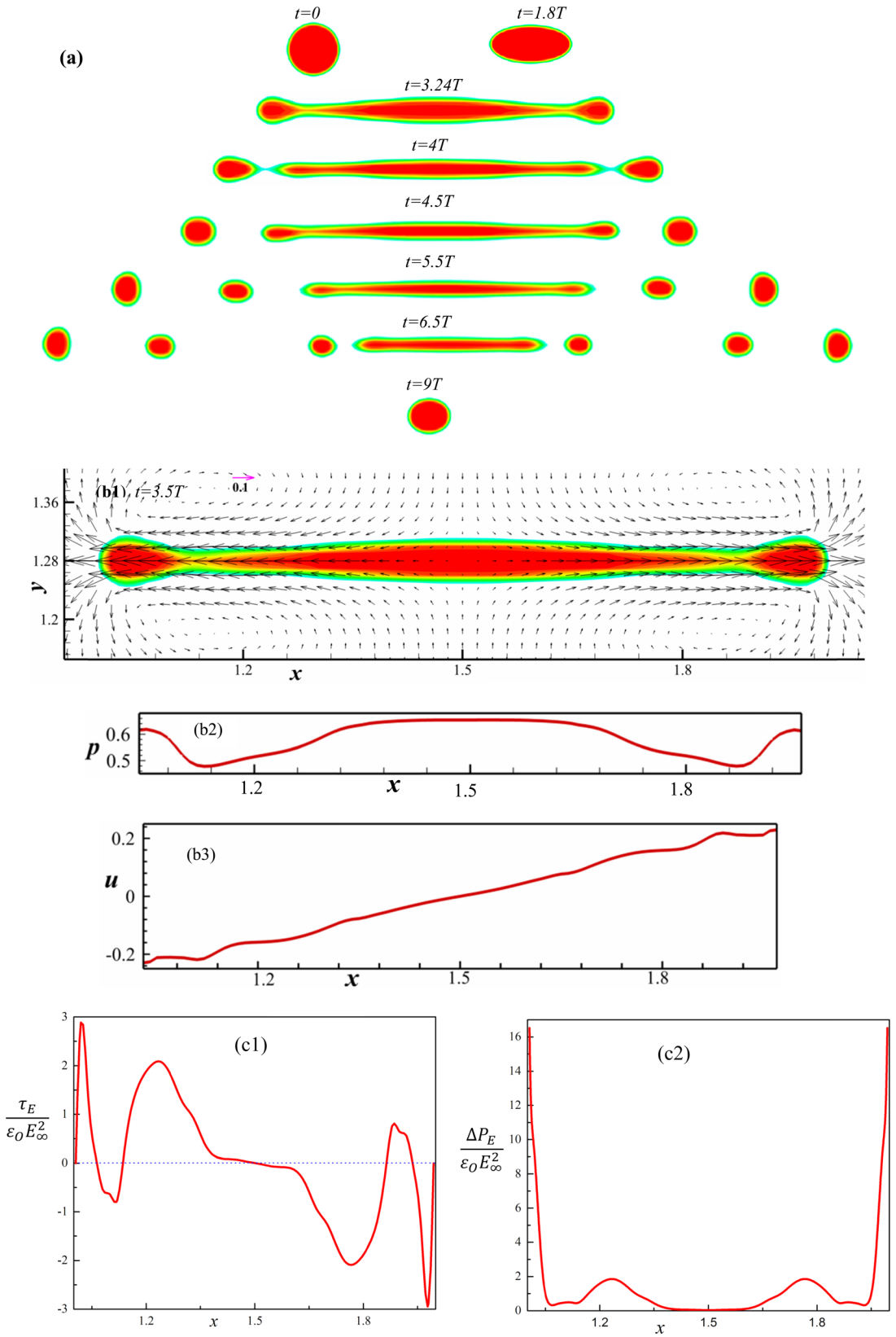

FIG. 9. (a) Transient evolution and breakup of a highly conducting drop at $R = 30$, $Q = 1.37$, $\lambda = 1$, $\mathrm{Ca}_E = 0.264$, and $\mathrm{Re} = 0.145$. (b1) Near-field flow behavior around an elongated drop during neck formation at $t = 3.5T$; (b2), (b3) extracted pressure and velocity distribution along the drop centerline at $t = 3.5T$. (c1), (c2) Distributions of nondimensional tangential electric stress and electric pressure on the drop surface at $t = 3.5T$.

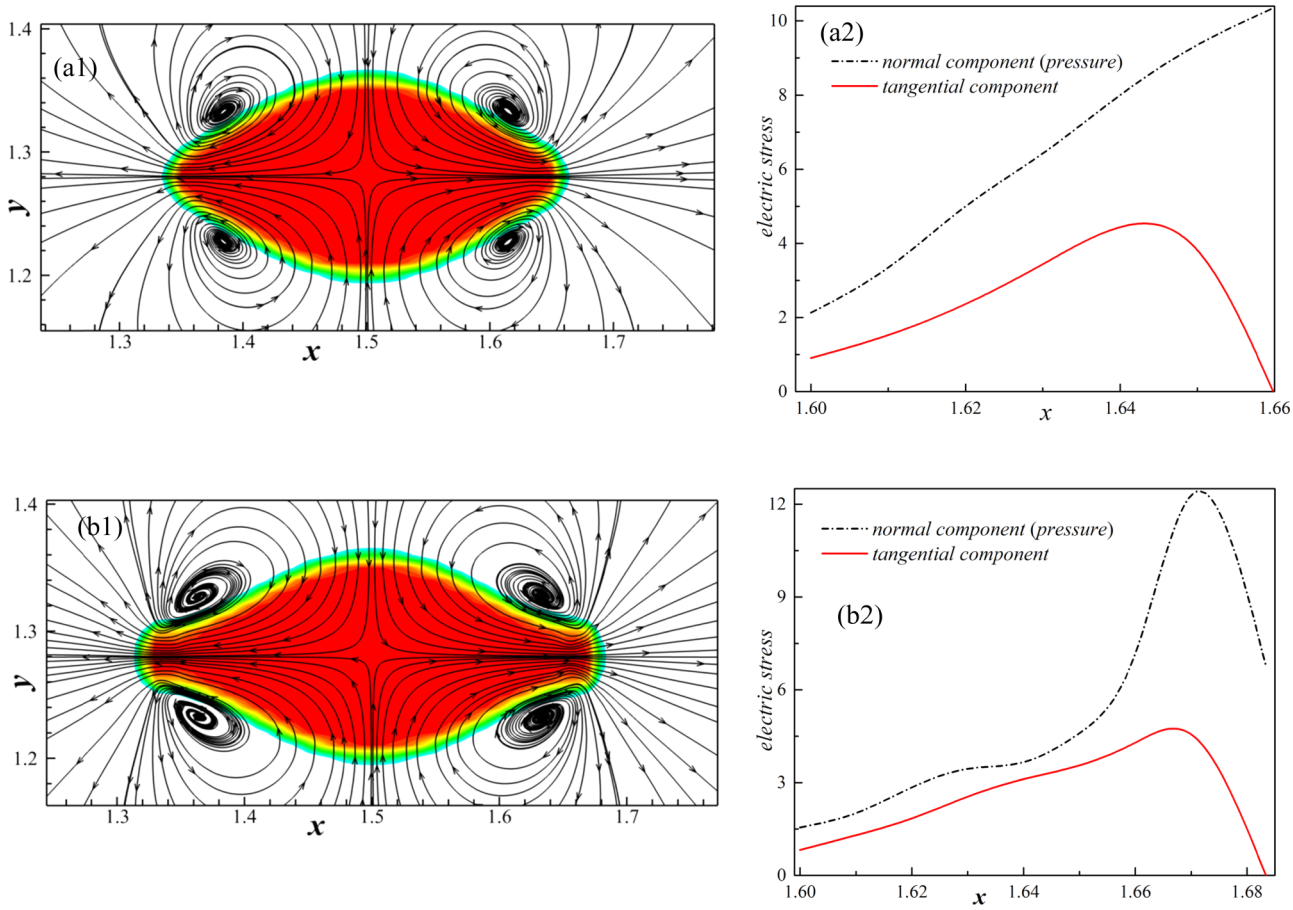

FIG. 10. Impact of varied Ca_E on modifying edge shape of a highly conducting drop. Deformed drop shape prior to onset of breakup, near-field flow behavior, and distribution of imposed electric stress along the right upper-half surface at $R = 30$, $Q = 1.37$, $\lambda = 1$. (a1), (a2) $Ca_E = 0.68$, Re $= 0.374$; (b1), (b2) $Ca_E = 0.83$, Re $= 0.457$.

to smoothen the tips, and create the open-jet-like local flow structure.

D. Influence of viscosity contrast

The preceding sections elaborate on drop-breakup phenomena for varied electric properties (Ca_E, Q, R) at fixed viscosity ratio $\lambda = 1$. While for small deformation [23–29] the viscosity ratio (λ) has limited effect, Lac and Homsy [23] studied the influence of λ on the stability of a leaky drop using the creeping flow approximation. In the present study, by taking into account the nonlinear inertial effects, the impact of varied λ on the breakup pattern and physics for the leaky drops is examined. For $\lambda = 0.087$, 5.0, 3.0, the detailed breakup behaviors are presented here; results broadly agree with recent measurements of Ha and Yang [15].

First, Fig. 11 shows physical evolution and breakup characteristics of an intermediately conducting drop ($R = 10$, $Ca_E = 0.89$) that has significantly lower viscosity ($\lambda = 0.087$) than the surrounding fluid, and displays patterns that are visibly consistent with the measurements reported by Ha and Yang [15] in their in Fig. 6 for the NH17 system. As Fig. 11(a) reveals, prior to breakup at $t = 7.5T$, the drop shape in elongation is characterized by the appearance of two fingertips at the ends, and the pinch-off occurs via the quadratic curved neck formations [46], in a way similar to one noted [Fig. 9(a), $Ca_E = 0.264$] for a highly conducting drop at a lower Ca_E. Distinctively though, after the first pair of daughter drops' pinch-off, the mother droplet [e.g., for $t \geqslant 10T$, Fig. 11(a)] at this lower viscosity ratio, $\lambda = 0.087$, continues to stretch further and releases a sequence of daughter drops, and eventually disintegrates (at $t = 17.5T$) into a stream of small drops rather than returning to a relaxed shape that is noted for a relatively high viscous drop [$\lambda = 1$, Fig. 9(a)].

For drop (fluid) viscosity significantly higher than the surrounding medium viscosity, i.e., at $\lambda = 5$, the breakup behavior or modes changed altogether. Figure 12(a) shows that the transient shape evolution plus breakup for a highly viscous intermediately conducting drop, at $\lambda = 5$ and $R = 10$, are characterized by the visibly longer stretching and the multiple neck formation ($t = 4.5T$) prior to pinch-off, whereby two long, thin threads connect the mother drop and two adjacent daughter drops. Moreover, the breakup for the highly viscous drop [Fig. 12(a), $\lambda = 5$] takes place significantly rapidly compared to a lowly viscous drop of $\lambda = 0.087 < 1$ [Fig. 11(a)], in which case much more viscous outer fluid dampens the droplet stretching process. Noteworthy also is that, unlike with $\lambda = 0.087$, for increased viscosity ratio $\lambda = 5$, following pinch-off at $t = 5T$ [Fig. 12(a)] of two pairs of daughter drops, the cylindrical mother droplet relaxes gradually to an

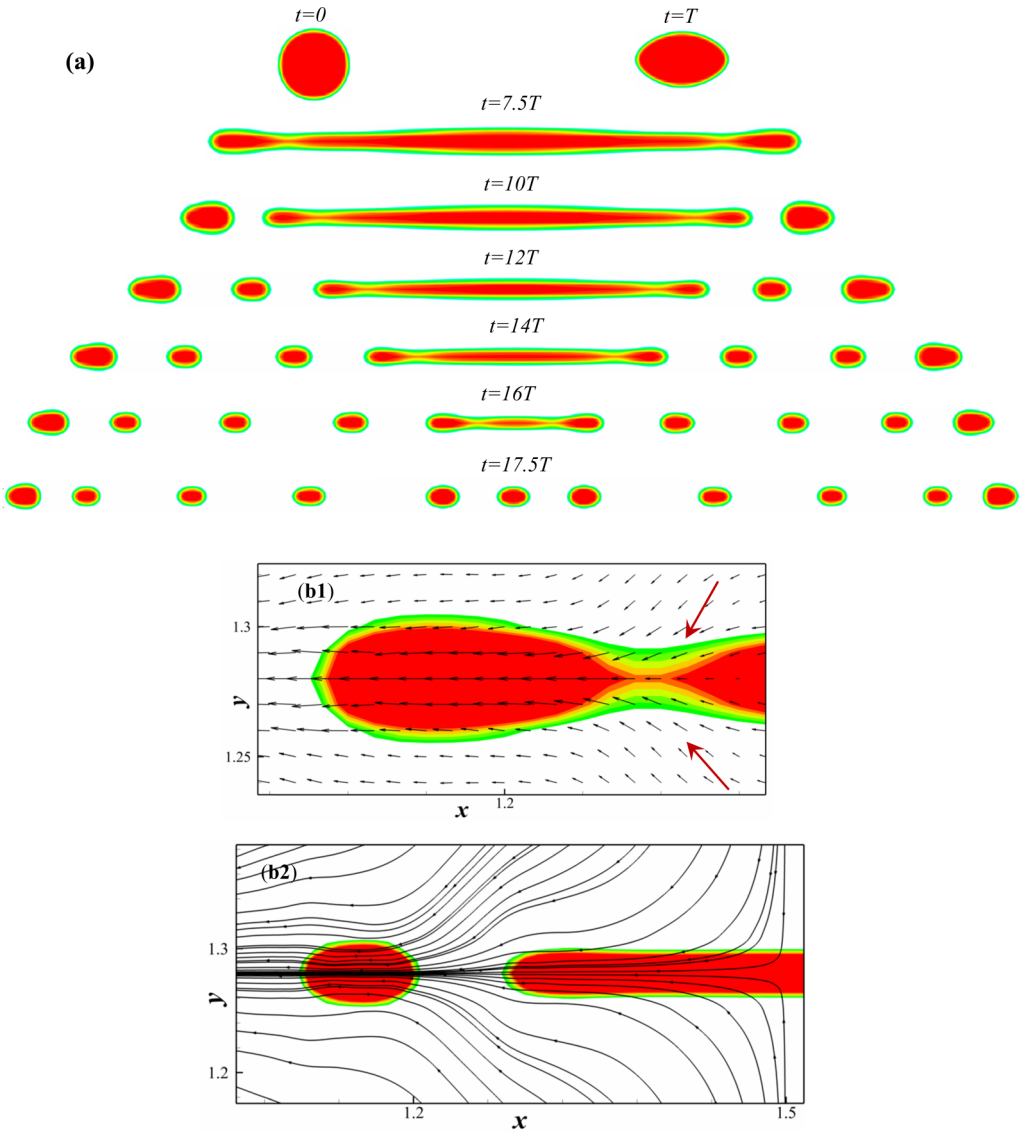

FIG. 11. Impact of reduced drop viscosity on breakup mode of an intermediately conducting drop. (a) Transient evolution of a drop in the process of breakup at $R = 10$, $Q = 1.37$, $\lambda = 0.087$, $\mathrm{Ca}_E = 0.89$, and $\mathrm{Re} = 0.015$. Close-up views of the neck region and induced flow: (b1) profile of the neck and generated velocity field prior to pinch-off, $t = 14T$; (b2) shapes of a daughter drop and curved edge of the mother drop following pinch-off, and near-field streamline pattern; $t = 14.5T$.

equilibrium status ($t = 9.5T$). Remarkably, Doshi *et al.* [46] also show that for increased drop viscosity the connecting neck elongates to a long, thin thread type shape (instead of a quadratic curve) as the breakup moment is approached. For clarity, Fig. 12(b1) presents a close view of a neck plus near-field flow behavior at $\lambda = 5$, in that a long, thin threadlike neck is clearly formed between the mother droplet and the adjacent daughter droplet on the left; which cconnects two conical ends at $t = 4.5T$. While the neck gets gradually thinner, the thread collapses at some point [e.g., at $t = 5T$, Fig. 12(a)] following the EHD interaction, and two daughter drop pairs are released. Note, in the process, the formation of two sharp high curvature conical ends on the mother droplet, at $\lambda = 5$. At this stage, the resulting high negative surface tension pressure, that is proportional to local curvature [46], counters the positive electric pressure, which is small here, as most of the charges are being taken away by daughter drops. This leads to eventual relaxation of the mother drop to an equilibrium shape (at $t = 9.5T$), while the daughter drops move toward distant boundaries. To reveal the detailed physics, Fig. 12(b2) shows inner flow behavior at one such sharp drop end, wherein a counter-rotating pair of inward moving *inflow* natured [34,47] vortices clearly dominate to manipulate the final relaxation status ($t = 9.5T$). In contrast, for a lowly viscous drop ($\lambda = 0.087$) as shown in Fig. 11(b1), the neck clearly becomes short, which is analogous to a quadratic curve shape, as revealed by Doshi *et al.* [46]. Around the relatively blunt neck [Fig. 11(b1)] the developed larger negative curvature induces the negative surface tension pressure that facilitates the capillary breakup, thus creating significant radial flow in the neck region. Moreover, quite distinctly from a highly viscous drop [Fig. 12(b2), $\lambda = 5$], as Fig. 11(b2) shows for a lower $\lambda = 0.087$, the developed round end curvature on the mother drop, upon the pinch-off

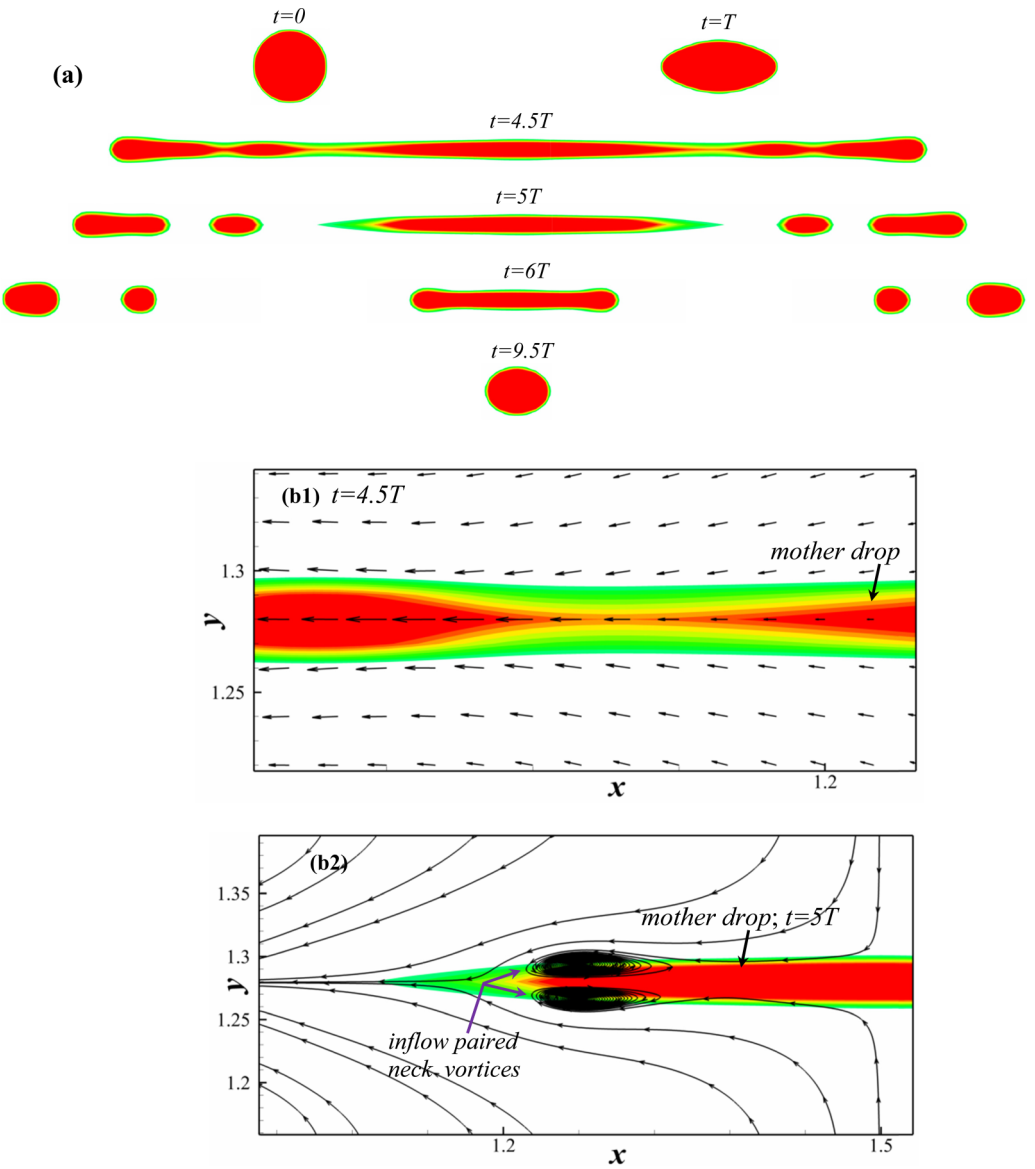

FIG. 12. Multilobed evolution and breakup of an intermediately conducting highly viscous leaky drop. (a) Transient evolution of drop shape in the process of breakup at $R = 10$, $Q = 1.37$, $\lambda = 5$, $\mathrm{Ca}_E = 0.67$, and $\mathrm{Re} = 0.73$. Close-up views of the neck region and induced flow: (b1) profile of a longer neck and generated velocity field prior to pinch-off; $t = 4.5T$; (b2) developed pointed edge shape of the mother drop following pinch-off, while the streamline pattern reveals dominance of an *inflow* type near-edge vortex pair in the mother drop upon breakup; $t = 5T$.

of daughter drops (at $t = 14.5T$), is incapable of inducing a gradual relaxation, as the required reversed flow near the round end (of the mother drop) could not be created in this case [that dominated for $\lambda = 5$, Fig. 12(b2)] accordingly a series of end-pinching daughter drops is gradually produced [see Fig. 11(a), $7.5T \leqslant t \leqslant 17.5T$].

However, the breakup behavior of a highly conducting drop ($R > 20$) is quite sensitive to the fluid viscosity. Figure 13 shows that, for $\lambda = 0.087 \ll 1$, only one type of end-pinching breakup mode persists at $R = 30$, $Q = 1.37$; this is found independent of Ca_E. The breaking events hereby evolve in a similar but faster process compared to an intermediately conducting drop [Fig. 11(a), $R = 10$]. Moreover, the maximum stretched length prior to initiation of breakup (at $t = 2.6T$, Fig. 13) for the highly conducting drop is shorter than that of an intermediately conducting drop [at $t = 7.5T$, Fig. 11(a)]. On the other hand, for increased viscosity (i.e., $\lambda > 2$) of highly conducting drops ($R = 30$) two types of breakup modes are detected as Ca_E is increased. For clarity, Fig. 14(a) displays the lobed end-pinching mode at $\lambda = 3$, $R = 30$, $Q = 1.37$, for a lower $\mathrm{Ca}_E = 0.4$ (< 0.6), whereas Fig. 14(b) shows formation of the pointed end shape at a higher $\mathrm{Ca}_E = 0.6$. Notably, the nonpointed end that emerged at around $\lambda \approx 1.0$ [Fig. 10(b1)] is no longer seen in these cases.

Remarkably, for leaky dielectrics [19,20] in addition to the *prolate* deformation, drops also deform to the *oblate* shape [34,48]. In such a situation EHD properties satisfy a relation $Q/R > 1$, and the two generated near-interface vortex pairs drive bulk outer fluid from pole to equator [34]. Furthermore

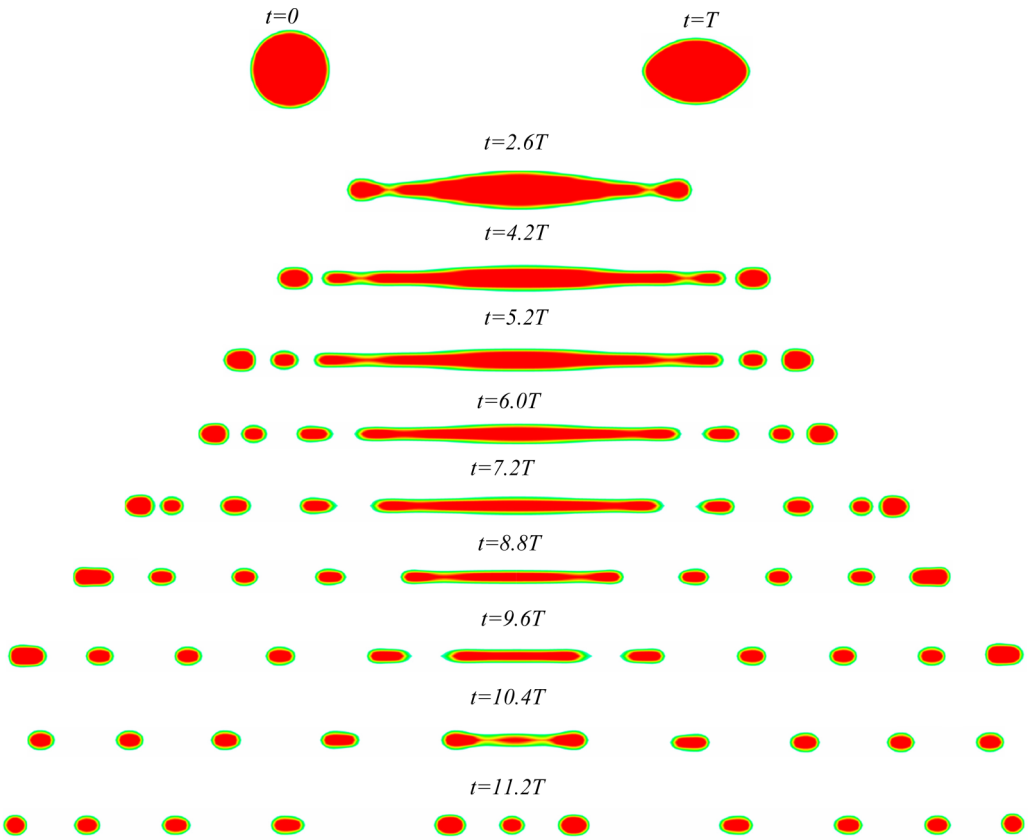

FIG. 13. Impact of reduced viscosity on the breakup pattern of a highly conducting drop. Time-dependent droplet evolution in the process of breakup at $R = 30$, $Q = 1.37$, $\lambda = 0.087$, $\mathrm{Ca}_E = 0.61$, and $\mathrm{Re} = 0.0047$.

the charge relaxation time ($\sim\varepsilon_{\mathrm{out}}/\sigma_{\mathrm{out}}$) of fluid surrounding an oblate drop appears shorter than that of a drop-fluid ($\sim\varepsilon_{\mathrm{in}}/\sigma_{\mathrm{in}}$), and a reversed surface charge distribution relative to that for $Q/R < 1$ is induced, causing formation of the electric dipole moment opposite to the applied electric field. In this circumstance, as electric field strength increases up to a threshold value for the applied uniform electric field, first the spontaneous three-dimensional electrorotation occurs prior to breakup [32,48–50]. Note that electrorotation of an oblate drop originates from the charge convection on the interface. Therefore, investigation of EHD behavior (electrorotation or breakup) of an oblately deformed drop in a stronger electric field requires altogether a different formulation, and is the focus of our next work. The interested reader may, however, refer to the existing slim volume of work [32,48–50] on electrorotation plus breakup of oblately deformed drops as placed in a strong electric field.

It may be worth mentioning at this point that the motion of liquid films in three dimensions (3D) can be influenced due to Rayleigh-Plateau (RP) instability, particularly in the absence of an electric field, whereby the pinching is driven by surface tension and a minimization of area. In the present case or geometry, such an instability is not possible. Nevertheless, we can compare the length and timescales over which the RP instability would develop and length scales of the presently investigated EHD drops as breakup is approached. Notably, Stone *et al.* [51,52] examined the breakup process of highly elongated (non-EHD) liquid drops to test the feasibility or presence of capillary wave instability and show that for drop extension ratio L/a (L and a being final extended length and radius of a drop) up to 15, *no capillary wave instability occurs*. However, in the present study, the maximum extension ratio (L/a) of an EHD drop is 13.5. Moreover, the timescale $t = 110.2$ that the capillary wave (instability) takes [52] to achieve sufficient amplitude (0.01) *is much larger* than the timescale $t = 54.0$ (as normalized using $t' = av\rho/\gamma$; the same method as in Stone *et al.* [52]) of the longest EHD end pinching detected in our study (e.g., Fig. 6), and as the applied electric field acts to expedite the end pinching. Accordingly, we expect that also in 3D liquid columns the EHD end pinching dominates over the RP instability.

IV. CONCLUSIONS

In this work, with incorporated full nonlinear inertial effects the detailed EHD breakup phenomena for the leaky dielectric drops in another immiscible leaky dielectric outer fluid are numerically investigated using the explicit forcing LBM model. The Ca_E-dependent stable drop deformation up to the threshold of breakup was previously studied using the linear theory, that is, the creeping flow approximation. We observe that the linear variation of drop deformation rate D and E^2 as predicted by Taylor's first-order theory is valid in a range of small deformation ($D < 0.1$). For higher deformation, dD/dE^2 deviates from the linear nature and increases nonlinearly and rapidly with Ca_E to reach a turning point at

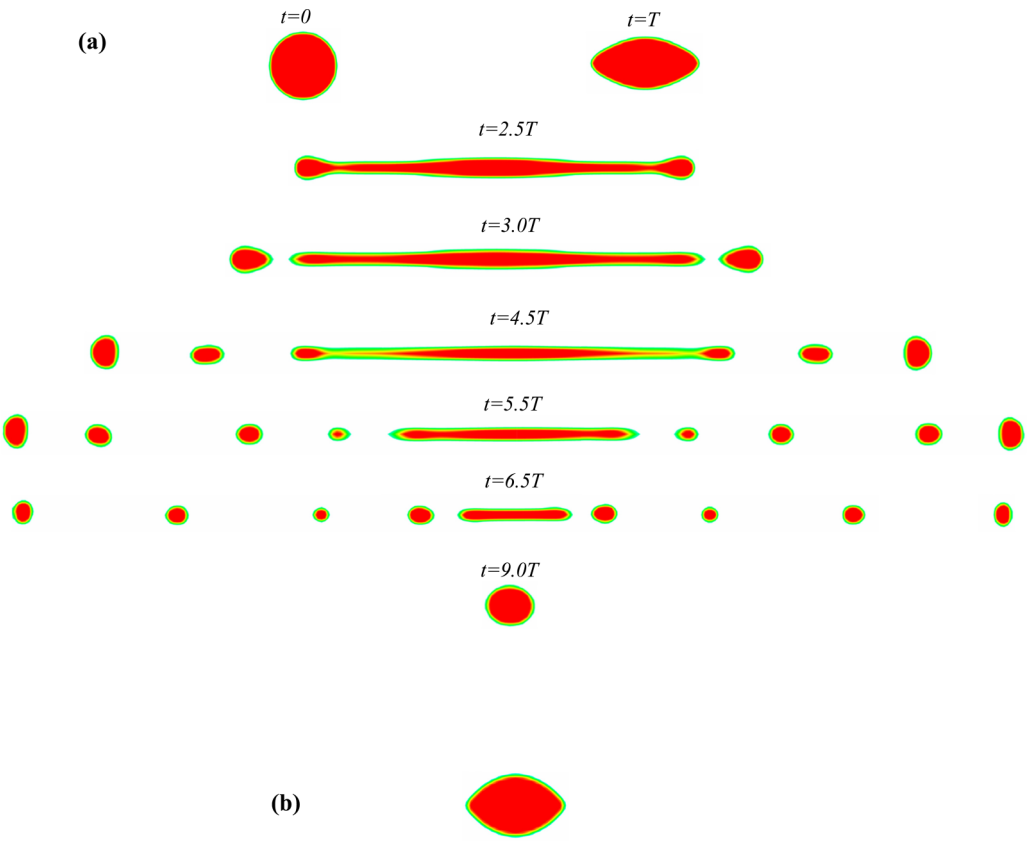

FIG. 14. Impact of increased drop viscosity on the breakup pattern of a highly conducting drop. (a) Transient drop evolution in the process of breakup at $R = 30$, $Q = 1.37$, $\lambda = 3$, $\mathrm{Ca}_E = 0.4$, and $\mathrm{Re} = 0.11$; (b) deformed drop shape with conical ends that occurred prior to breakup at higher $\mathrm{Ca}_E = 0.6$ and $R = 30$, $Q = 1.37$, $\lambda = 3$, $\mathrm{Re} = 0.165$.

which a slight increase of the electric field intensity causes a sudden drop elongation (especially for lower permittivity ratios $Q = 0.1,\ 1.37$), and the transitioning drop evolves from an ellipsoidal shape to an elongated, slender two-lobe shape.

Based on transition characteristics, first, at a fixed viscosity ratio $\lambda = 1$, we demonstrate explicit breakup modes and governing physics for varied conductivity ratio R of a drop, i.e., for slightly conducting ($R < 10$), intermediately conducting ($10 \leqslant R \leqslant 20$), and highly conducting ($R > 20$) cases, while the adopted nonlinear model effectively provides clear physical insight into end-pinching breakup of an elongated state. Since the EHD breakup is an unstable dynamic process led by interacting electric field and induced fluid motion, for a leaky dielectric drop as it evolves to a slender shape most of the electric charges accumulate at two bulbous tips. Our simulated results reveal that the dominant driving force for EHD drop stretching is the generated *high positive electric pressure at the tips*. Accordingly, the induced fluid in the drop ends is pulled to move faster (via imposed electric pressure) in opposite directions than that in an intermediate bulbous section, wherein the *tangential electric stress drives the drop stretching mechanism* despite its lower strength. The resulting difference of local drop extension rates thereby leads to the formation of necks, and the phenomenon is unambiguously characterized via the detected rapid local increase of the centerline velocity gradient and the symmetrical growth of intermediate inflection points in the tangential electric stress profile. Meanwhile, the generated negative curvature around the necks creates local low pressure regions that facilitate capillary breakup. Notably, a slightly conducting drop of $R = 5$ (<10) displays the end-pinching breakup at a lower $Q = 0.05$ (<1), which produces a single pair of daughter drops. For higher $Q = 1.37$, while the size of the ejected daughter drops appears bigger, the breakup pattern remains invariable with $\mathrm{Ca}_E > \mathrm{Ca}_{E,c}$. However, the intermediately conducting leaky drops of $10 \leqslant R \leqslant 20$ exhibit variable breakup patterns with increased Ca_E, although at a lower $Ca_E = 0.55$ ($>Ca_{E,critic}$) the global breakup feature remains similar to that of a slightly conducting one ($R < 10$). For Ca_E increased to 0.83 an intermediately conducting ($R = 10$) drop reveals *multiple* pinching neck formations, and the resulting two pairs of symmetrical daughter drops are released in the breakup process. Importantly, a highly conducting ($R = 30$) leaky drop displays a breakup pattern that resembles that of a *perfectly conducting drop*, and the fluid permittivity (Q) has little influence. Notably, our simulated $\mathrm{Ca}_{E,\mathrm{critical}}$'s for the onset of breakup for three highly conducting leaky drops at fixed $R = 30$ and with varied $Q = 0.1,\ 1.37,\ 10.0$ appear as 0.219, 0.219, 0.227, respectively, which remain closely consistent to around 0.22, as predicted previously. However, here we uncover three different types of transitional drop shapes prior to breakup (at $R = 30$) and display the dominance of three distinct breakup modes with increasing Ca_E: namely, via formation of lobes ($\mathrm{Ca}_E \leqslant 0.66$), pointed ends ($0.66 < \mathrm{Ca}_E < 0.83$), and nonpointed ends ($\mathrm{Ca}_E \geqslant 0.83$).

The viscosity ratio λ is noted to significantly alter both the breakup pattern as well as near-tip flow physics. At high viscosity ratio $\lambda = 5$, the transitional shape prior to pinch-off of a moderately conducting drop ($R = 10$) is characterized by the presence of the multiple necks, and the particularly long, thin neck formation between a mother drop and the two to-be-released adjacent daughter drops is detected, which connects two conical ends of the mother drop. Following pinch-off of two pairs of daughter drops the created sharp high curvature ends in this case ($\lambda = 5$) lead an elongated mother drop to relax to an asymptotic equilibrium shape, by virtue of the imposed high surface tension pressure and induced forcing that is effectively produced via the inward dynamics of two $inflow$ paired neck vortices. Distinctly, for a lowly viscous moderately conducting drop of $\lambda = 0.087$ and $R = 10$, the breakup event is as follows: First, a pair of shorter quadratic curved or lobed necks develop prior to pinch-off, and the resulting high radial pressure difference between inside and outside fluid facilitates the capillary breakup. Upon pinch-off of a pair of daughter drops the mother droplet experiences

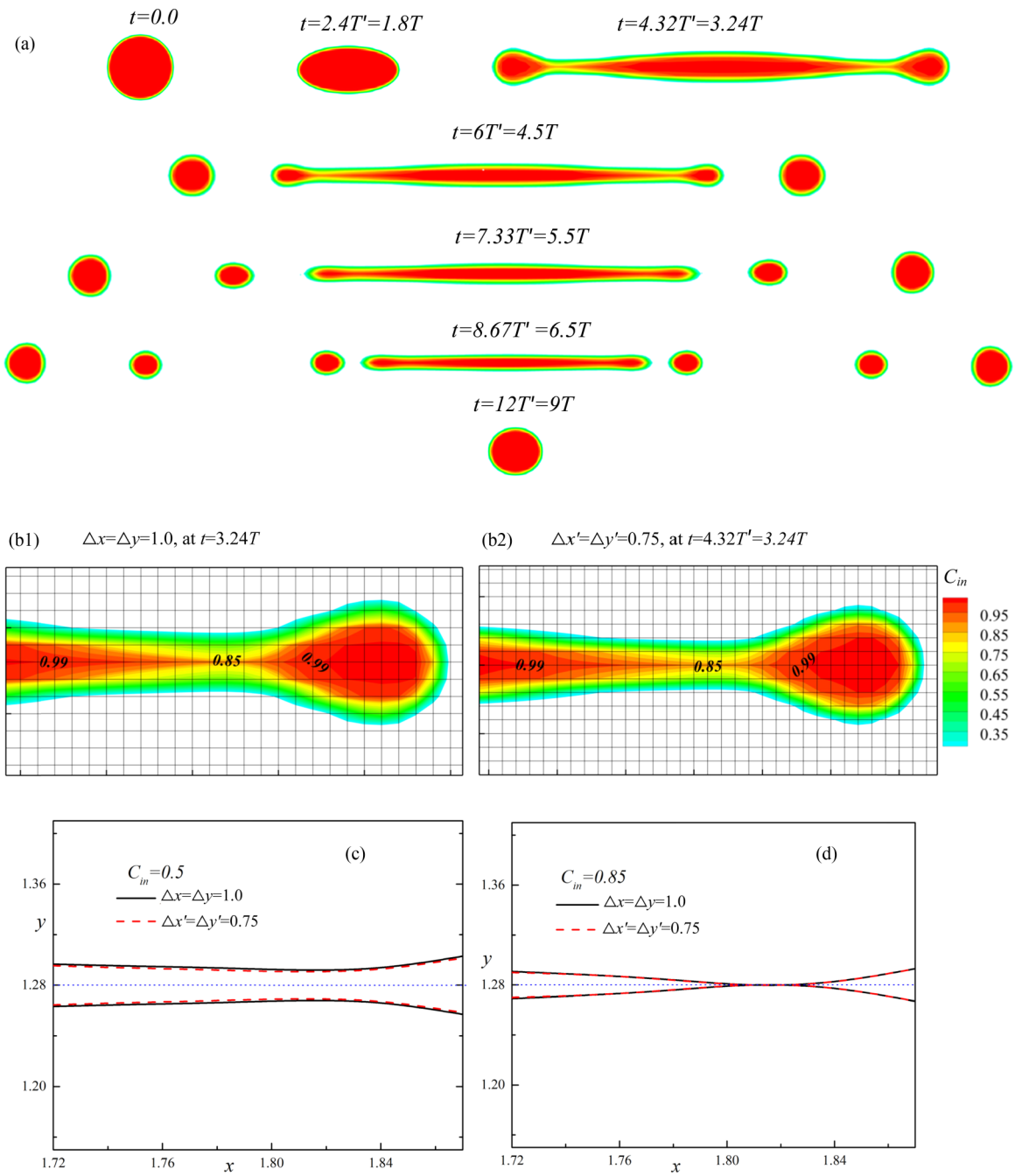

FIG. 15. (a) Invariance of breakup sequence at $R = 30.0$, $Q = 1.37$, $\lambda = 1.0$, and $\mathrm{Ca}_E = 0.264$ (with respect to Fig. 9) on a refined lattice spacing, where, $T' = 100\Delta t' = 0.75T$. (b1), (b2) Close-ups of grid resolution in the neck region for two different adopted lattices. (c) The neck interface for two different lattices, as defined by $C_{\mathrm{in}} = 0.5$ curves. (d) Coincidence of neck shape for two different lattices, at a near threshold $C_{\mathrm{in}} = 0.85$.

fresh elongation and evolves via newly formed two-lobed ends attached by quadratic curved necks, and gradually disintegrates into a stream of smaller drops due to recurrent release of daughter drops. At $\lambda = 0.087$, the generated outward hydrodynamic thrust by accrued charges at the symmetric round ends on the mother drop, upon the daughter drop's pinch-off, prohibits the mother drop from attaining an asymptotically relaxed state.

In addition, the viscosity ratio λ significantly influences the breakup behavior of a highly conducting ($R = 30$) drop. At $\lambda = 0.087$ ($\ll 1$) only one breakup mode via lobe pinching persists for the highly conducting ($R = 30$) case, for Ca_E exceeding a critical magnitude. On the other hand, at $\lambda = 1$, three different drop-breakup modes are detected, which evolve through growths of lobed ends at a lower $\mathrm{Ca}_E = 0.264$, pointed conical type ends at an intermediate $\mathrm{Ca}_E = 0.68$, and nonpointed curved ends at higher $\mathrm{Ca}_E = 0.83$. However, for $\lambda = 3(>2)$ the nonpointed end mode is suppressed, and the lobed-end mode directly transits to the pointed conical-end mode for increased Ca_E.

ACKNOWLEDGMENT

The work is supported by NRF Grant No. 2017R1D1A1A09000952, South Korea.

APPENDIX: INVARIANCE OF DROPLET EJECTION AND NECK FORMATION

Herein the lattice size–independent behaviors of neck formation and droplet pinch-off via lobes are reexamined for the case $R = 30.0$, $Q = 1.37$, $\lambda = 1.0$, $\mathrm{Ca}_E = 0.264$, presented in Fig. 9, by using a refined domain ($\Delta x' = 0.75\Delta x$, $\Delta y' = 0.75\Delta y$, Δx, Δy being the original lattice spacing) and keeping all other relevant simulation parameters invariable in order to display consistent interface deformation and breakup processes. First, Fig. 15(a) shows a simulated drop-breakup pattern for the finer lattice which reveals that the breakup sequence converges to the one presented in Fig. 9(a), and end pinching contributes to the breakup. Second, Figs. 15(b1) and 15(b2) show the close-ups of the neck region for two different grid resolutions. We may add here that, in the interparticle potential LBM model [34,35] the thickness [39] of a drop interface that separates two immiscible fluids always occupies three lattices (which is the same number of grids used to define the interface in another method, such as VOF and level set [13,28]), no matter how refined the grid or lattice spacing is. To be precise, the neck region is identified here in terms of $0.5 \leqslant C_{\mathrm{in}}[=\rho_{\mathrm{in}}/(\rho_{\mathrm{in}} + \rho_{\mathrm{out}})] < 0.99$ in xy space. The axial neck length is determined by the x distance between two neighboring points on the central line, where $C_{\mathrm{in}} = 0.99$ occurs. Note that the axial length of the neck ($15\Delta x = 20\Delta x'$) in two cases is equal [see Figs. 15(b1) and 15(b2)]. Third, to clearly compare the simulated neck shapes under varied grid resolutions, in Figs. 15(c) and 15(d) we plot contours of two density fractions $C_{\mathrm{in}} = 0.5$ (denotes the interface) and $C_{\mathrm{in}} = 0.85$ (detected near-threshold density fraction in the neck). Importantly, the C_{in}-dependent widths (expressed as a function of position) of the neck region in the two cases exactly coincide [Fig. 15(d)] for $C_{\mathrm{in}} = 0.85$ (a near-threshold value), and the maximum local error is only 0.128% [Fig. 15(c)] for $C_{\mathrm{in}} = 0.5$. Accordingly, the lattice spacing adopted in the study is sufficient to unfold the EHD drop-breakup phenomenon.

[1] O. A. Basaran, H. Gao, and P. P. Bhat, Nonstandard inkjets, Annu. Rev. Fluid. Mech. **45**, 85 (2013).
[2] G. I. Taylor, Disintegration of water drops in an electric field, Proc. R. Soc. London, Ser. A. **280**, 383 (1964).
[3] G. I. Taylor, Electrically driven jets, Proc. R. Soc. London, Ser. A. **313**, 453 (1969).
[4] T. C. Scott, Use of electric fields in solvent extraction: A review and prospectus, Sep. Purif. Methods **18**, 65 (1989).
[5] C. I. Christov and G. M. Homsy, Enhancement of transport from drops by steady and modulated electric fields, Phys. Fluids. **21**, 083102 (2009).
[6] H. A. Stone, A. D. Stroock, and A. Ajdari, Engineering flows in small devices: Microfluidics toward a lab-on-a-chip, Annu. Rev. Fluid Mech. **36**, 381–411 (2004).
[7] C. Y. O'Konski and H. C. Thacher, Jr., The distortion of aerosol droplets by electric field, J. Phys. Chem. **57**, 955 (1953).
[8] C. Y. O'Konski and F. E. Harris, Electric free energy and the deformation of droplets in electrically conducting systems, J. Phys. Chem. **61**, 1172 (1957).
[9] M. J. Miksis, Shape of a drop in an electric field, Phys. Fluid. **24**, 1967 (1981).
[10] O. A. Basaran and L. E. Scriven, Axisymmetric shape and stability of charged drops in an electric field, Phys. Fluids A **1**, 799 (1989).
[11] C. T. R. Wilson and G. T. Taylor, The bursting of soap bubbles in a uniform electric field, Proc. Camb. Philos. Soc. **22**, 728 (1925).
[12] J. D. Sherwood, Breakup of fluid droplets in electric fields and magnetic field, J. Fluid Mech. **188**, 133 (1988).
[13] H. Paknemat, A. R. Pishevar, and P. Pournaderi, Numerical simulation of drop deformations and breakup modes caused by direct current electric fields, Phys. Fluids **24**, 102101 (2012).
[14] S. Torza, R. G. Cox, and S. G. Mason, Electrohydrodynamic deformation and burst of liquid drops, Philos. Trans. R. Soc. London, Ser. A. **269**, 295 (1971).
[15] J. W. Ha and S. M. Yang, Deformation and breakup of Newtonian and non-Newtonian conducting drops in an electric field, J. Fluid Mech. **405**, 131 (2000).
[16] N. Dubash and A. J. Mestel, Breakup behavior of a conducting drop suspended in a viscous fluid subject to an electric field. Phys. Fluids **19**, 072101 (2007).
[17] N. Dubash and A. J. Mestel, Behaviour of a conducting drop in a highly viscous fluid subject to an electric field, J. Fluid Mech. **581**, 469 (2007).
[18] R. B. Karyappa, S. D. Deshmukh, and R. M. Thaokar, Breakup of a conducting drop in a uniform electric field, J. Fluid Mech. **754**, 550 (2014).

[19] G. I. Taylor, Studies in electrohydrodynamics. I. the circulation produced in a drop by electric field, Proc. R. Soc. London, Ser. A. **291**, 159 (1966).
[20] J. R. Melcher and G. I. Taylor, Electrohydrodynamics: a review of the role of interfacial shear stresses, Annu. Rev. Fluid Mech. **1**, 111 (1969).
[21] O. Vizika and D. A. Saville, The electrohydrodynamic deformation of drops suspended in liquids in steady and oscillatory electric fields, J. Fluid Mech. **239**, 1 (1992).
[22] O. O. Ajayi, A note on Taylor's electrohydrodynamic theory, Proc. R. Soc. London, Ser. A. **364**, 499 (1978).
[23] E. Lac and G. M. Homsy, Axisymmetric deformation and stability of a viscous drop in a steady electric field, J. Fluid Mech. **590**, 239 (2007).
[24] J. C. Baygents, N. J. Rivette, and H. A. Stone, Electrohydrodynamic deformation and interaction of drop pairs, J. Fluid Mech. **368**, 359 (1998).
[25] J. Q. Feng and T. C. Scott, A computational analysis of electrohydrodynamics of a leaky dielectric drop in an electric field, J. Fluid Mech. **311**, 289 (1996).
[26] J. Hua, L. K. Lim, and C. H. Wang, Numerical simulation of deformation/motion of a drop suspended in viscous liquids under influence of steady electric fields, Phys. Fluids. **20**, 113302 (2008).
[27] R. Pillai, J. D. Berry, D. J. Harvie, and M. R. Davidson, Electrolytic drops in an electric field: a numerical study of drop deformation and breakup, Phys. Rev. E **92**, 013007 (2015).
[28] G. Tomar, D. Gerlach, G. Biswas, N. Alleborn, A. Sharma, F. Durst, S. W. J. Welch, and A. Delgado, Two-phase electrohydrodynamic simulation using a volume of fluid approach, J. Comput. Phys. **227**, 1267 (2007).
[29] J. Zhang and D. Y. Kwok, A 2D lattice Boltzmann study on electrohydrodynamic droplet deformation with the leaky dielectric theory, J. Comput. Phys. **206**, 150 (2005).
[30] R. T. Collins, J. J. Jones, M. T. Harris, and O. S. Basaran, Electrohydrodynamic tip streaming and emission of charged drops from liquid cones, Nat. Phys. **4**, 149 (2008).
[31] H. Nganguia, A. T. Layton, M. C. Lai, and W. F. Hu, Electrohydrodynamics of a viscous drop with inertia, Phys. Rev. E **93**, 053114 (2016).
[32] D. Das and D. Saintillan, Electrohydrodynamics of viscous drops in strong electric fields: numerical simulations, J. Fluid Mech. **829**, 127 (2017).
[33] D. A. Saville, Electrohydrodynamics: the Taylor-Melcher leaky dielectric model, Annu. Rev. Fluid Mech. **29**, 27 (1997).
[34] Q. Dong and A Sau, Electrohydrodynamic interaction, deformation, and coalescence of suspended drop pairs at varied angle of incidence, Phys. Rev. Fluids **3**, 073701 (2018).
[35] M. L. Porter, E. T. Coon, Q. Kang, J. D. Moulton, and J. W. Carey, Multicomponent interparticle potential lattice Boltzmann model for fluids with large viscosity ratios, Phys. Rev. E **86**, 036701 (2012).
[36] Q. Li, K. H. Luo, Q. J. Kang, Y. L. He, Q. Chen, and Q. Liu, Lattice Boltzmann method for multiphase flow and phase-change heat transfer, Prog. Energy Combust. Sci. **52**, 62 (2016).
[37] Q. Kang, D. Zhang, and S. Chen, Displacement of a two-dimensional immiscible droplet in a channel, Phys. Fluids **14**, 3203 (2002).
[38] S. Hou, X. Shan, Q. Zou, G. D. Doolen, and W. E. Soll, Evaluation of two lattice Boltzmann models for multiphase flows, J. Comput. Phys. **138**, 695 (1997).
[39] Q. Kang, D. Zhang, and S. Chen, Displacement of a three-dimensional immiscible droplet in a duct, J. Fluid Mech. **545**, 41 (2005).
[40] N. S. Martys and H. Chen, Simulation of multicomponent fluids in complex three-dimensional geometries by the lattice Boltzmann method, Phys. Rev. E **53**, 743 (1996).
[41] X. He and N. Li, Lattice Boltzmann simulation of electrochemical system, Comput. Phys. Commun. **129**, 158 (2000).
[42] Z. Guo, T. S. Zhao, and Y. Shi, A lattice Boltzmann algorithm for electro-osmotic flows in microfluidic devices, J. Chem. Phys. **122**, 144907 (2005).
[43] S. Succi, *The Lattice Boltzmann Equation* (Oxford University Press, Oxford, 2001).
[44] J. U. Brackbill, D. B. Kothe, and C. Zemach, A continuum method for modeling surface tension, J. Comput. Phys. **100**, 335 (1992).
[45] M. R. Swift, W. R. Osborn, and J. M. Yeomans, Lattice Boltzmann Simulation of Nonideal Fluids, Phys. Rev. Lett. **75**, 830 (1995).
[46] P. Doshi, I. Cohen, W. W. Zhang, M. Siegel, P. Howell, O. A. Basaran, and S. R. Nagel, Persistence of memory in drop breakup: the breakdown of universality, Science **302**, 1185 (2003).
[47] A. Sau, Role of streamwise dynamics in spreading and mixing of flows through a rectangular sudden expansion, Phys. Fluids **23**, 083602 (2011).
[48] J. W. Ha and S. M. Yang, Electrohydrodynamics and electrorotation of a drop with fluid less conductive than that of the ambient fluid, Phys. Fluids **12**, 764 (2000).
[49] J. Q. Feng, A 2D electrohydrodynamic model for electrorotation of fluid drops, J. Colloid Interface Sci. **246**, 112 (2002).
[50] H. Sato, N. Kaji, T. Mochizuki, and Y. H. Mori, Behavior of oblately deformed droplets in an immiscible dielectric liquid under a steady and uniform electric field, Phys. Fluids **18**, 127101 (2006).
[51] H. A. Stone, B. J. Bentley, and L. G. Leal, An experimental study of transient effects in the breakup of viscous drops, J. Fluid Mech. **173**, 131 (1986).
[52] H. A. Stone and L. G. Leal, Relaxation and breakup of an initially extended drop in an otherwise quiescent fluid, J. Fluid Mech. **198**, 399 (1989).